The Pennsylvania State University

The Graduate School

Department of Aerospace Engineering

AN EXPERIMENTAL AND COMPUTATIONAL APPROACH TO ICED WIND TURBINE AERODYNAMICS

A Thesis in

Aerospace Engieering

by

Peter M. Blasco

© 2015 Peter M. Blasco

Submitted in Partial Fulfillment
of the Requirements
for the Degree of

Master of Science

May 2015

The thesis of Peter M. Blasco was reviewed and approved* by the following:

Sven Schmitz
Assistant Professor, Aerospace Engineering
Thesis Advisor

Jose Palacios
Assistant Professor, Aerospace Engineering

George Lesieutre
Professor, Aerospace Engineering
Head of the Department of Aerospace Engineering

*Signatures are on file in the Graduate School

ABSTRACT

This thesis presents an analysis of power loss of a representative 1.5 MW wind turbine for variable icing conditions. Power losses are estimated using aerodynamic data obtained in a combination of two experimental methods. Atmospheric icing conditions varying in temperature, droplet size, and liquid water content are generated in an icing facility to simulate a 45-minute icing event on a representative wind turbine airfoil section. The ice shapes are then molded for preservation and subsequent wind-tunnel testing. Lift and drag measurements are made and used to estimate the total power production of the iced wind turbine using a blade-element momentum theory prediction code. Detailed measurements of ice profiles show that aerodynamic penalties are mainly a function of surface roughness due to icing. A 16% loss of airfoil lift at operational angle of attack is observed for freezing-fog conditions. Drag increases at a lift coefficient of 0.5 are observed to be 190% at temperatures near 0°C, 145% near -10° C, and 80% near -20°C. An analysis of the wind turbine aerodynamic loads due to atmospheric icing yields power losses ranging from 16% to 26% near an average wind speed of 8 m/s. An exception to these results exists for a single super-large droplet icing case in which lift decrease and drag increase are more severe at 25% and 219%, respectively. The analysis gives insight to potential control strategies for wind turbine operators attempting to minimize revenue loss in cold-climate operations.

TABLE OF CONTENTS

List of Figures vi

List of Tables ix

Acknowledgements x

Chapter 1 Introduction 1

- Literature Review 2
  - Review of Numerical Studies 2
  - Experimental Studies 3
  - Field Observations 4
- Research Objectives 4
  - Thesis Chapter Overview 5

Chapter 2 Selection of Experimental and Computational Conditions 7

- Selection of a Representative Wind Turbine 7
- Icing Conditions 11

Chapter 3 Experimental and Computational Methods 14

- Experimental Properties 14
- Ice Shape Generation 16
  - LEWICE Validation Testing 18
  - Ice Accretion Experiments 19
- Ice Shape Preservation and Casting 22
  - Surface Roughness Measurements 30
- Wind Tunnel Testing 31
  - Wind-Tunnel Validation Testing 35
  - Wake Survey Correction Method 40
- Performance Prediction Using XTurb-PSU 42

Chapter 4 Results and Discussion 46

- Ice Accretion Tests 46
- Wind Tunnel Tests 50
- Power Prediction with XTurb-PSU 54
- Discussion of Results 59
  - Potential Correlations 59
  - Operational Strategies for Optimal Performance 60
  - Potential Applications of Data 64

Chapter 5 Conclusion 65

Future Work 66
References 68
Appendix A LEWICE Ice Accretion Plots 72
Appendix B Iced Airfoil Tabulated Polar Data 79
Appendix C XTurb-PSU Input Files 86
Appendix D Ice Casting Photographs 96

LIST OF FIGURES

Figure 2-1. PSU 1.5 MW wind turbine torque distribution at V_{Wind} = 12 m/s. 8

Figure 2-2. Generic and modified airfoil distributions. 9

Figure 2-3. PSU-Ice 1.5MW torque distribution at V_{Wind} = 11 m/s. 10

Figure 2-4. Power curve comparison. 11

Figure 2-5. NCAR icing conditions envelope. 12

Figure 3-1. Chain of experimentation for iced airfoil performance measurement. 14

Figure 3-2. Rotor test blade. 15

Figure 3-3. Adverse Environment Rotor Test Stand (AERTS at Penn State) 17

Figure 3-4. LEWICE accretion for Case 3 in Table 2-3. 19

Figure 3-5. Top view schematic of AERTS facility. 20

Figure 3-6. Rime Ice - LWC: 0.21 g/m³, MVD: 20μm, T: -21°C, Time: 2 min. 21

Figure 3-7. Glaze ice - LWC: 0.45 g/m³, MVD: 18μm, T: -3° C, Time: 15 min. 22

Figure 3-8. Aluminum molding box with DU 93-W-210 airfoil blade section. 23

Figure 3-9. Mold pouring at -12° C. 24

Figure 3-10. DU 93-W-210 blade section: glaze ice mold. 25

Figure 3-11. Precision template with sunken bolts aligned for a casting. 26

Figure 3-12. Wind-tunnel model with mounted ice shapes. 27

Figure 3-13. View of wind-tunnel model transition region. 28

Figure 3-14. Microscope view of leading-edge rime ice compared to a millimeter scale. 29

Figure 3-15. Leading-edge ice at the transition from the smooth to rough zones. 29

Figure 3-16. Precision measurements of ice surface roughness. 30

Figure 3-17. DU 93-W-210 airfoil with glaze ice mounted in the wind tunnel. 31

Figure 3-18. Wake survey setup with Pitot tube for calibration. 33

Figure 3-19. Wake Survey Measurement at 4° Angle of Attack 34

Figure 3-20. Validation of lift measurements for an S-805 airfoil [27]. 36

Figure 3-21. Comparison of drag measurements for an S-805 airfoil. 37

Figure 3-22. Comparison of lift measurements for the clean DU 93-W-210 airfoil. 38

Figure 3-23. Comparison of load cell drag measurements for the clean DU 93-W-210 airfoil. 39

Figure 3-24. Drag difference between load cell and wake survey measurements. 41

Figure 3-25. XTurb-PSU cover page. 42

Figure 3-26. Lift and drag comparisons for modified XTurb-PSU airfoil input data. 44

Figure 3-27. PSU-Ice 1.5MW angle of attack distribution at a wind speed of 8 m/s. 45

Figure 4-1. Icing zone diagram. See Table 4-1 for descriptions of zones. 47

Figure 4-2. Photo of icing roughness. 48

Figure 4-3. DU 93-W-210 airfoil: lift vs. angle of attack. 51

Figure 4-4. DU 93-W-210 airfoil: lift coefficient vs. drag coefficient. 52

Figure 4-5. DU 93-W-210 airfoil: Curve fits of lift coefficient vs. drag coefficient. 53

Figure 4-6. Power loss results from XTurb-PSU 55

Figure 4-7. Angle of attack distributions for Region II and Region III wind speeds 56

Figure 4-8. Power loss within Region II for the PSU-Ice 1.5MW wind turbine. 57

Figure 4-9. Power loss within Region III for the PSU-Ice 1.5MW wind turbine. 58

Figure 5-1. Power curve for optimally controlled pitch for icing Case 3 (Table 2-3) 62

Figure 5-2. Root-flap bending moment for icing Case 3 (Table 2-3) at different pitch settings. 63

Figure A-1. Refer to Table 2-3: Case 1. 73

Figure A-2. Refer to Table 2-3: Case 2. 74

Figure A-3. Refer to Table 2-3: Case 3. 75

Figure A-4. Refer to Table 2-3: Case 4. 76

Figure A-5. Refer to Table 2-3: Case 5. 77

Figure A-6. Refer to Table 2-3: Case 6.....78

Figure D-2. Surface roughness detail. Refer to Table 2-3: Case 1. 96

Figure D-3. Surface roughness detail. Refer to Table 2-3: Case 2. 97

Figure D-4. Surface roughness detail. Refer to Table 2-3: Case 3. 97

Figure D-4. Surface roughness detail. Refer to Table 2-3: Case 4. 98

Figure D-5. Surface roughness detail. Refer to Table 2-3: Case 5. 98

Figure D-6. Surface roughness detail. Refer to Table 2-3: Case 6. 99

LIST OF TABLES

Table 2-1. Airfoil distribution information for Figure 2-2. 10

Table 2-2. PSU-Ice 1.5MW baseline information. 11

Table 2-3. Icing Conditions 13

Table 3-1. Flowfield Properties 16

Table 4-1. Zone Descriptions for Figure 4-1. 47

Table 4-2. Ice Dimensions normalized by the chord length. 49

Table 4-3. Quantified Performance Penalties for each icing case. 59

Table B-1. Airfoil Polar Data for the clean DU 93-W-210 airfoil. 79

Table B-2. Airfoil Polar Data for case 1 (Table 2-3) for the DU 93-W-210 airfoil. 80

Table B-3. Airfoil Polar Data for case 2 (Table 2-3) for the DU 93-W-210 airfoil. 81

Table B-4. Airfoil Polar Data for case 3 (Table 2-3) for the DU 93-W-210 airfoil. 82

Table B-5. Airfoil Polar Data for case 4 (Table 2-3) for the DU 93-W-210 airfoil. 83

Table B-6. Airfoil Polar Data for case 5 (Table 2-3) for the DU 93-W-210 airfoil. 84

Table B-7. Airfoil Polar Data for case 6 (Table 2-3) for the DU 93-W-210 airfoil. 85

ACKNOWLEDGEMENTS

I would like to acknowledge Dr. Sven Schmitz and Dr. Jose Palacios for their dedication to my research efforts throughout my two years as a graduate student. Both Dr. Schmitz and Dr. Palacios significantly contributed to my knowledge and skills as an engineer and I am grateful to have studied under their direction. I acknowledge Yiqiang Han for his immense help in using the AERTS facility and teaching me about all things icing. I acknowledge Matt Drury for his efforts designing the test blades used in experiments for this thesis. I acknowledge Rick Auhl for his supervision of use of the Hammond low-speed wind tunnel and assistance in setting up wind-tunnel experiments. I acknowledge Dr. Mark Maughmer for his consultation, guidance, and advice on wind-tunnel testing. I also acknowledge Penn State students Emily Gerhart, Taylor Hoover, Samuel Kulp, Neel Sheth, Lucas Willson, and Cheng Zhang for their assistance performing experiments as well as Mark DeAngelo for assistance taking photographs. This research was sponsored by the National Center for Atmospheric Research (NCAR) in conjunction with XCEL Energy, and we thank those organizations for the opportunity to perform this work. Finally, I acknowledge and thank my friends and family for their support throughout my efforts as a graduate researcher.

Chapter 1

Introduction

Wind turbines are becoming increasingly prevalent and important in the generation of renewable energy around the world. Wind energy generating capacity in the US has increased from 2500 MW in 1999 to 28,500 MW in early 2009 [1]. The growth of the wind industry is leading to an increased interest in wind farms in cold climate regions both in Northern Europe and North America [2]. These cold climate regions expose wind turbines to atmospheric icing conditions, which can result in multiple wind farm icing events during the winter season. Many studies show that these events lead to severe power degradation [2-16]. This results in large losses of revenue for wind turbine operators during the winter season and an Annual Energy Production (AEP) loss of up to 20% [5]. In addition to revenue lost by reduced AEP, costs can be incurred due to inaccurate power forecasting and penalties associated with grid integration [17].

The driving force behind these power losses is degradation of airfoil performance due to icing. In an icing event, super-cooled water droplets accrete to wind turbine blades, causing an alteration to both the shape and surface roughness of local blade airfoil sections [13, 18]. The aerodynamic changes associated with these alterations are well understood for aircraft airfoil geometries. Bragg gives an excellent review of iced airfoil aerodynamics, discussing the decrease in lift and increase in drag on the airfoil section for various types of ice [19]. However, aerodynamic penalties can be different for different airfoil geometries under the same icing conditions and less investigation has been given to wind turbine airfoils [19]. The lack of reliable aerodynamic data for iced wind turbine airfoils is illustrated by a recent study by Laasko et al. that suggests additional research is needed to better predict the aerodynamic penalties associated with particular icing

conditions [4]. This gap of information and burgeoning interest in cold climate wind farms is the motivation behind this research.

Literature Review

There have been many studies related to aircraft and rotorcraft icing dating back to the late 1920's [19]. However, icing studies related to wind turbines are less prevalent and are still in stages of discovery and learning. The studies range from numerical simulations of wind turbine power loss, experimental quantification of aerodynamic losses, and actual measurements of losses at wind energy sites. The following sections review recent research from each of these categories.

Review of Numerical Studies

Many recent studies of the changes in wind turbine performance are investigated with the use of computational simulations of both ice accretion and aerodynamics [6, 7, 10, 11, 16, and 20]. The ice accretion simulations provide accurate ice shapes, but must be supplemented with smoothing functions and surface roughness parameters to obtain the correct surface roughness. The surface roughness information is critical to predicting the correct drag of the iced airfoil because small changes in surface roughness can yield dramatic differences in airfoil performance. At times, the surface roughness can be more significant than the actual size, shape, and placement of the accreted ice [16]. Switchenko et al., in regard to FENSAP-ICE (a commonly used wind turbine ice accretion and aerodynamic solver), suggest that more research is needed in the area of surface-roughness effects for particular icing conditions [16]. This conclusion motivates the study of this thesis to find detailed aerodynamic performance data for particular icing conditions on a commonly used wind turbine airfoil.

In addition to issues with unreliable surface roughness-information, numerical simulations can produce different aerodynamic results depending on the solver being used. Even with ice properties held constant, a comparative study of various RANS solvers yielded differences in airfoil performance depending on the type of turbulence modeling (specifically in the glaze ice regime) [20]. Attempting to numerically simulate the multi-phase flowfield about an iced wind turbine rotor is a difficult and computationally expensive task. Information provided in this thesis can help validate results obtained by these complex solvers.

Experimental Studies

Other research on wind turbine performance degradation due to icing includes experimental studies of many types [3, 9, 10, 13, and 15]. Similar to numerical studies, some of these experimental studies use ice accretion codes to generate simulated ice shapes for experimental wind-tunnel or water-tunnel testing [3, 13]. Once again, roughness must be simulated on these shapes by grit, and the aerodynamic drag results differ depending on the chosen k/c value [13]. These studies accurately document the aerodynamic performance of the grit roughness, but lose accuracy in predicting drag of the true ice roughness.

Other studies experimentally generate actual ice shapes for aerodynamic analysis [9,10]. However, the chosen airfoils for these studies (S809 [9] and NACA 64-415 [10]) are for stall-regulated wind turbines at lower operational Reynolds number and will have different aerodynamic characteristics than an airfoil designed for a utility-scale pitch-controlled wind turbine. These experiments provide valuable insight into the physics of ice accretion and the unique icing properties of wind turbine blade geometries. The assortment of data at similar icing conditions to the research performed in this thesis is important for comparison and validation of results.

Field Observations

Some of the most valuable data available on wind turbine icing is from actual wind farms operating in cold climates. However, these data are difficult to analyze for wind turbines due to the large time scale of wind turbine power generation and the many variables involved. Some researchers have been able to analyze the data and publish summaries of power losses [2, 4, 5, and 8].

A study of particular interest is from Gillenwater et al. regarding the energy losses at Canadian wind energy sites during the winter season [8]. The study integrated data collected over four years of wind farm operations at two separate sites. The study concluded that average power losses of 26% to 27% are observed and that "operation procedures during an icing event should be modified in order to reduce the risks (of performance losses) and maximize production [8]." The conditions at these sites are very similar to conditions replicated in this research and are suited for comparison of experimental results. The end goal of the research presented here is to fulfill Gillenwater et al.'s request by exploring operating procedures that reduce the risks of performance losses and maximize production based on detailed aerodynamic performance data.

Research Objectives

This thesis presents a combined experimental and computational effort to predict wind turbine performance changes due to ice accretion at various representative atmospheric conditions. The focus of this effort is to obtain accurate aerodynamic data by generating ice on a representative utility-scale wind turbine airfoil in an ice accretion facility and mold the ice shapes for subsequent wind-tunnel testing. The experiments are designed in order match Reynolds number as close as possible to the flowfield properties of a utility-scale wind turbine. The changes in airfoil

performance characteristics are measured to provide a comparison of aerodynamic penalties for varying icing parameters. The aerodynamic information is finally used as an input to a wind turbine performance analysis code to yield power losses for the icing conditions and to provide initial data for operational strategies.

The following tasks will be conducted:

1. Design a utility-scale wind turbine suitable for analysis based on experiments carried out on a representative airfoil.
2. Choose properties for ice accretion and wind tunnel experiments based on the designed wind turbine and icing condition recommendations from the project sponsor.
3. Perform ice accretion experiments and preserve ice shapes by molding and casting them.
4. Perform wind-tunnel experiments on preserved ice shapes to obtain lift and drag data for the representative wind turbine airfoil.
5. Computationally predict power loss on the representative wind turbine using experimental iced-airfoil data. Then provide an analysis of the power loss and strategies for mitigating power loss before, during, and after an icing event.

Thesis Chapter Overview

This thesis is organized into the following remaining chapters:

Chapter 2: Selection of Experimental and Computational Conditions: The conditions for experimentation are defined by designing a representative wind turbine and choosing an airfoil for experimentation.

Chapter 3: Experimental and Computational Method: The experimental and computational method for determining wind turbine power loss is described in detail. This includes descriptions of ice accretion experiments, wind tunnel experiments, and XTurb-PSU calculations.

Chapter 4: Results and Discussion: Results from ice accretion tests, wind tunnel tests, and XTurb-PSU calculations are presented objectively. The implications of the results are then discussed as well as their potential applications.

Chapter 5: Conclusion: The work done in this thesis is summarized along with major results from the experiments and computational analysis. Recommendations for future work based on results and observations during experiments are also presented.

Chapter 2

Selection of Experimental and Computational Conditions

This research requires replicating flow conditions over a wind turbine blade for two different experimental disciplines: icing and aerodynamics. Each of these disciplines is governed by its own unique scaling laws and associated experimental limitations. Combining experimental methods requires careful attention to both types of scaling. A compromise is made, which allows for experimentation at the edge of both the icing and aerodynamic envelope.

The following section on research design gives details on how the final experimental conditions are chosen. The basic icing and aerodynamic conditions of the research are defined. A utility-scale wind turbine is designed and modified to allow for experimentation on a primary airfoil. The design of the generic wind turbine using XTurb-PSU and the selection of icing conditions give flow field and icing parameters for use in ice accretion and wind-tunnel testing experiments.

Selection of a Representative Wind Turbine

This research attempts to quantify aerodynamic losses for a typical utility-scale wind turbine. A 1.5 MW power output is determined to be representative of the utility-scale with a GE 1.5sle wind turbine representing a typical example. A generic 1.5MW wind turbine, the PSU 1.5MW, created in XTurb-PSU is used as a baseline for selecting airfoils for testing. The airfoils on the PSU 1.5MW wind turbine are from the Delft University dedicated wind turbine airfoil family. These airfoils are used by wind turbine manufacturers worldwide and provide excellent

performance characteristics to pitch-controlled wind turbines in the 30 to 100 meter rotor diameter range [21].

To test as many icing conditions as possible, only one airfoil is selected for ice accretion experiments and subsequent wind-tunnel testing. The DU 93-W-210 airfoil is chosen because its radial location on the turbine blade typically spans much of the region of maximum torque generation (see Figure 2-1). The full airfoil distribution for the PSU 1.5MW wind turbine is also displayed in Figure 2-2a.

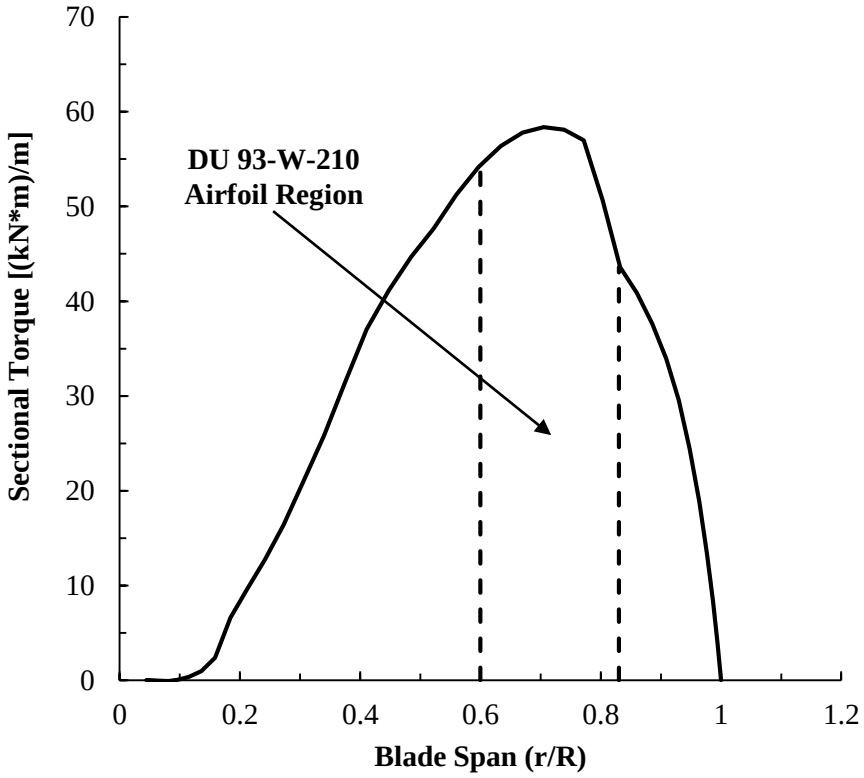

Figure 2-1. PSU 1.5 MW wind turbine torque distribution at V_{Wind} = 12 m/s.

The choice of only one blade airfoil motivated the design of a custom 1.5 MW Horizontal Axis Wind Turbine for analysis. As mentioned previously, this turbine is designed to be similar to a GE 1.5 MW wind turbine [22]. The design starts with the PSU 1.5MW airfoil distribution

displayed in Figure 2-2a. This airfoil distribution is then modified so that the DU 93W-210 airfoil is the primary airfoil and spans the majority of the torque generating portion of the blade. The inner 40% region is spanned by cylinder bodies and two root Delft airfoils (see Figure 2-2b). The torque distribution in Figure 2-3 for this modified airfoil distribution shows that the inner airfoils only generate 16% of the torque at rated wind speed, so aerodynamic penalties on these airfoils due to icing are neglected. Setting the primary airfoil at the 40% span location also avoids power calculations at high angles of attack near the root, which is outside the range of measured iced wind-tunnel airfoil data in this research.

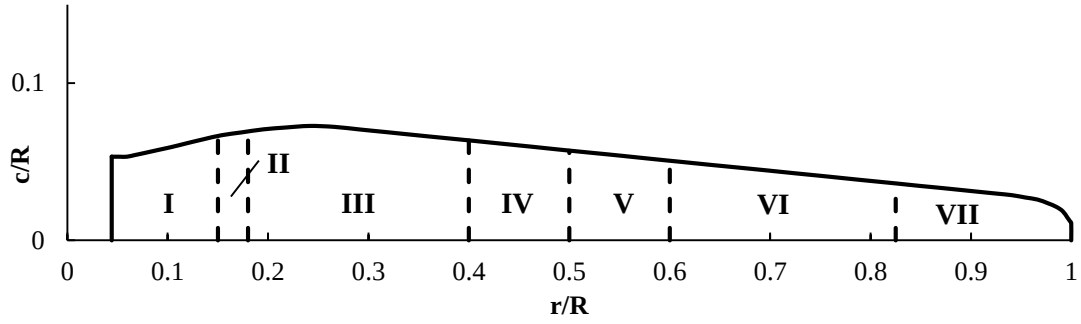

a) Original airfoil distribution (PSU 1.5MW).

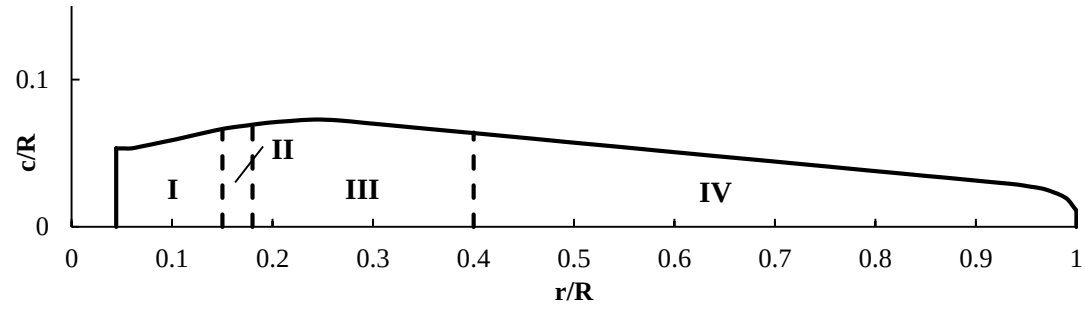

b) Modified airfoil distribution (PSU-Ice 1.5MW).

Figure 2-2. Generic and modified airfoil distributions.

Table 2-1. Airfoil distribution information for Figure 2-2.

Blade Span Location	I	II	III	IV	V	VI	VII
a) DU Airfoil	Cylinders	00-W2-401	00-W2-350	97-W-300	91-W2-250	93-W-210	95-W-180
b) DU Airfoil	Cylinders	00-W2-401	00-W2-350	93-W-210	N/A	N/A	N/A

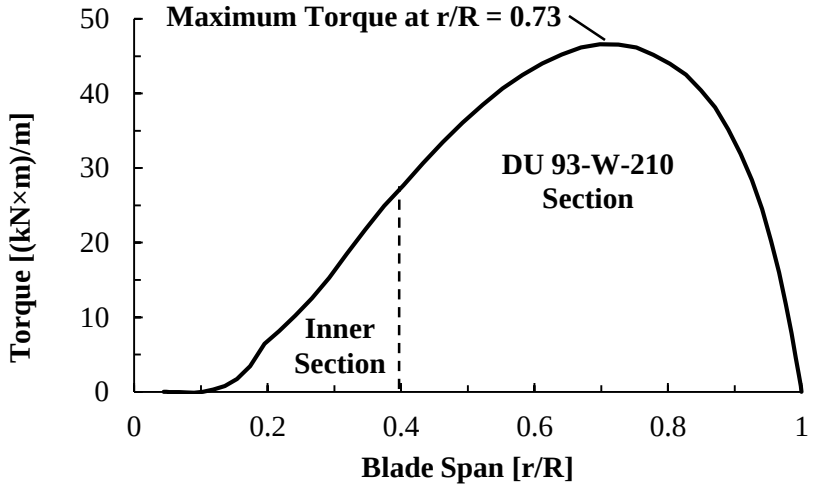

Figure 2-3. PSU-Ice 1.5MW torque distribution at V_{Wind} = 11 m/s.

A comparison of power curves for the PSU-Ice 1.5MW wind turbine is displayed in Figure 2-4. It is clear that the modified airfoil distribution results in only small changes between the power curves. The PSU-Ice 1.5MW wind turbine performs slightly better than its predecessor because of the aerodynamic benefits of the (relatively) thin DU 93-W-210 airfoil. This yields a slightly lower rated wind speed, but the power curve still agrees well with the GE 1.5sle [22]. Therefore, the modified airfoil distribution for the PSU-Ice 1.5MW wind turbine (see Table 2-2 for technical specifications and Appendix C for the XTurb-PSU geometry input file) is representative of a typical utility-scale wind turbine. The design of this wind turbine using XTurb-PSU allows for the generation of local flowfield and blade geometry properties given a wind speed and radial location on the blade. This information is used to define experimental conditions, which are described in more detail in a later section.

Table 2-2. PSU-Ice 1.5MW baseline information.

Number of Blades	3
Rotor Diameter	77 m
Rated Capacity	1,500 kW
Cut-in Wind Speed	2 m/s
Cut-out Wind Speed	25 m/s
Rated Wind Speed	11 m/s
Tip Speed Ration Range	2.2 – 13.9
Power Control	Blade Pitch Control

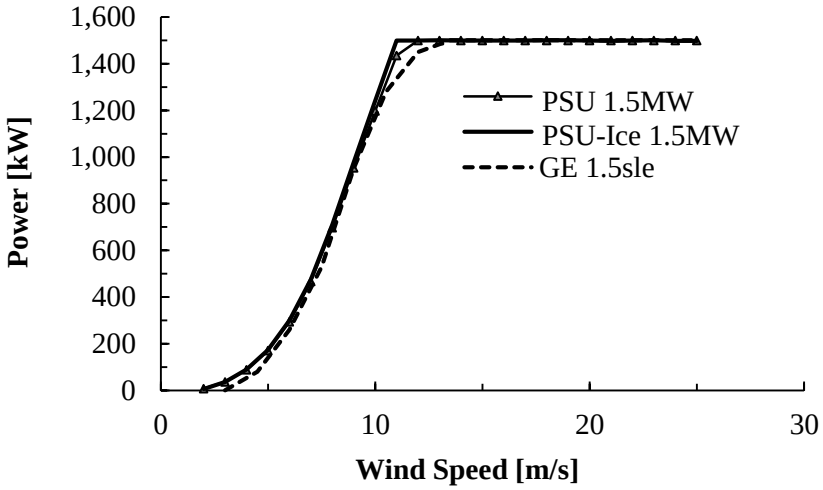

Figure 2-4. Power curve comparison.

Icing Conditions

Icing conditions for this research were suggested by collaborators at the National Center for Atmospheric Research (NCAR). The conditions are selected to be representative of freezing fog conditions encountered in the Great Plains region of the Northern United States. The cases are also selected to give reasonable comparisons between the three standard icing reference variables: Liquid Water Content (LWC), Median Volumetric Diameter (MVD), and Temperature (T). The

first variable, LWC, is a measure of the concentration of super-cooled water droplets in the air. The second variable, MVD, is a measure of droplet size. The LWC, MVD, droplet impact velocity, and temperature each affect the physics of ice accretion in different ways. The LWC and MVD tend to affect the thickness of accreted ice shapes, while temperature and droplet impact velocity affects the local roughness, severity of ice feathers, and adhesion strength of the ice [18].

The conditions suggested by NCAR were a spread of low LWC and MVD values representing the values typical of freezing fog (see Figure 2-5). Initially, it was intended to define cases at each region suggested by NCAR. However, applying scaling laws to these full-scale conditions limited the testing envelope to the facility envelope displayed in Figure 2-5 due to testing facility limitations (see Chapter 3: Ice Accretion Experiments). The actual physics and details of scaling icing conditions are discussed in Chapter 3.

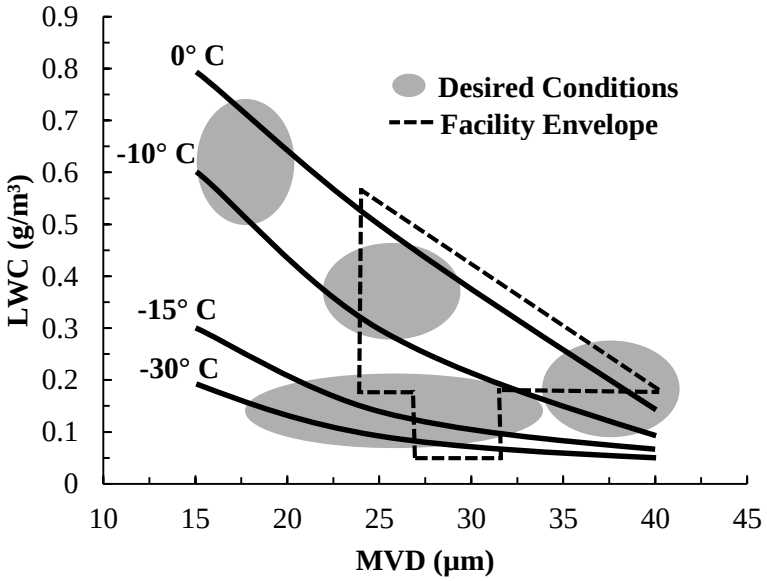

Figure 2-5. NCAR icing conditions envelope.

Six cases are selected from the facility envelope in Figure 2-5 and displayed in Table 2-3. Five of these conditions represent the aforementioned freezing fog type ice along with an exception

case. The exception case is to experiment with super large droplet (SLD) ice accretion, which is representative of a freezing drizzle type condition. The icing event time is chosen to be 45 minutes for all cases. This event time is long enough to accrete ice shapes with significant roughness, but little deviation in large-scale shape between cases. This is the optimal condition for comparing surface roughness characteristics of the different types of ice. Changes due to scaling are also displayed in Table 2-3 and are discussed further in Chapter 3.

Table 2-3. Icing Conditions

Field Conditions					
Case	**Ice Type**	**LWC (g/m³)**	**MVD (µm)**	**T (°C)**	**Time (mm:ss)**
1	Freezing Fog	0.1	28	-21.3	45:00
2	Freezing Fog	0.22	25	-10.8	45:00
3	Freezing Fog	0.22	30	-9.7	45:00
4	Freezing Fog	0.24	33	-4.5	45:00
5	Freezing Fog	0.48	33	-2.3	45:00
6	Freezing Drizzle	0.26	250	-8.1	45:00
Facility Scaled Conditions					
Case	**Ice Type**	**LWC (g/m³)**	**MVD (µm)**	**T (°C)**	**Time (mm:ss)**
1	Freezing Fog	0.12	16	-21.5	13:42
2	Freezing Fog	0.255	14.5	-11	13:54
3	Freezing Fog	0.255	17	-9.9	14:00
4	Freezing Fog	0.255	19	-4.7	14:36
5	Freezing Fog	0.453	19	-2.5	15:36
6	Freezing Drizzle	0.295	143	-8.3	14:12

Chapter 3

Experimental and Computational Methods

The previous chapter focused on the selection of conditions for experimentation and design of a wind turbine for computational analysis. This chapter focuses on the experiments themselves as well as the final step of analyzing experimental data using XTurb-PSU. The basic process of determining total wind turbine power production for a given icing condition is displayed in Figure 3-1. This figure gives the general overview of processes, which will be described in further detail.

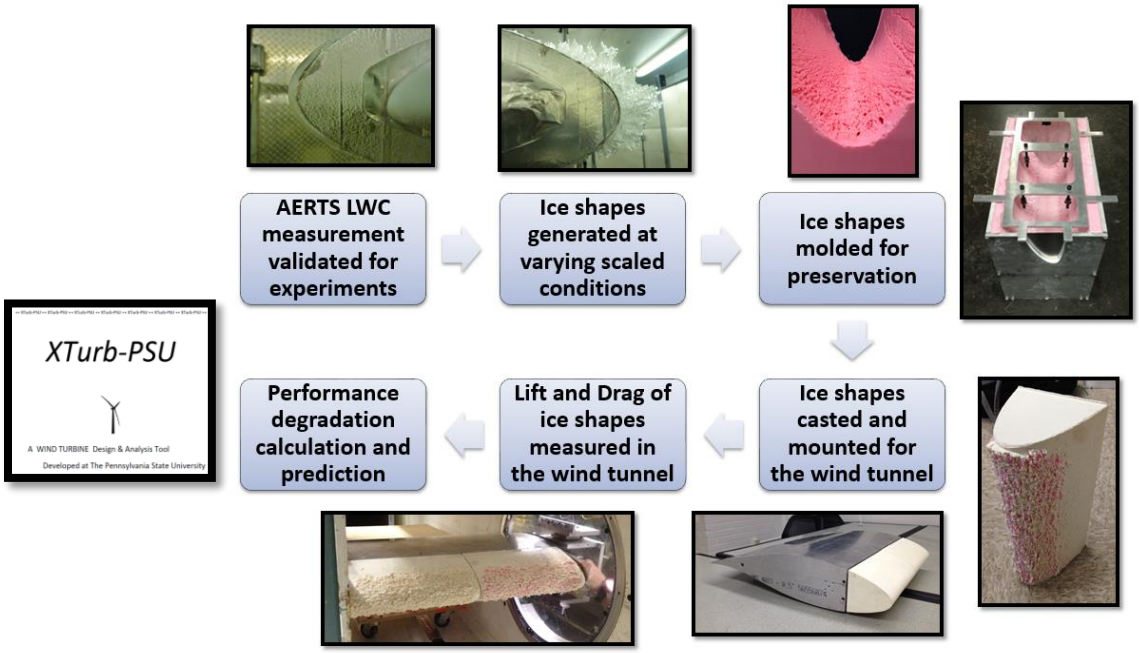

Figure 3-1. Chain of experimentation for iced airfoil performance measurement.

Experimental Properties

Experimental flow properties are based on the local flow properties near the region of maximum torque at a Region II wind speed of 8 m/s. Table 3-1 displays these properties along with

the properties that were used in the experiments. Based on these flow properties and limitations of the ice accretion facility, a half-scale chord blade is used for experimentation. The half-scale rotor blade, illustrated in Figure 3-2, carries a 28.5 in chord by 12 in span DU 93-W-210 airfoil section at its tip.

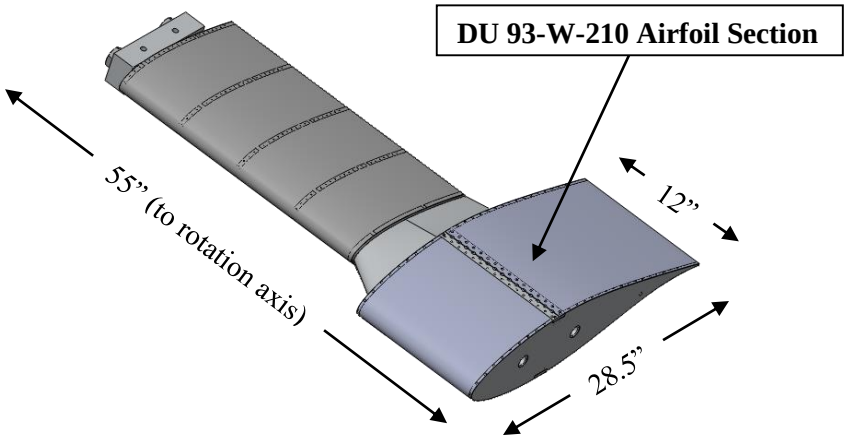

Figure 3-2. Rotor test blade.

As displayed in Table 3-1, experimental relative velocity is 41 m/s, which is 9m/s less than the full-scale velocity. The maximum velocity is 41 m/s due to structural limitations of the rotorstand and blades. An angle of attack of 0° is used in experimentation because vibrations on the rotorstand exceeded acceptable values at higher angles of attack. This discrepancy between 0° and 5° angle of attack will result in small changes in ice shape due to the low ice accretion time (roughly 15 minutes) and low LWC of the experiments (see Appendix A for comparisons of simulated ice accretion shapes at 0° and 5° angle of attack). Surface roughness details are of highest concern and are preserved through the discrepancy in ice accretion angle of attack. Reynolds number remains on the same order throughout experimentation at 1.5 to 2.4 million. Although the full-scale Reynolds number is 4.9 million, icing surface roughness reduces the effects of changing Re on aerodynamic performance [19]. Therefore, at these high Reynolds numbers, acceptable dynamic similitude is considered to be achieved throughout the experimentation.

Table 3-1. Flowfield Properties

Wind turbine Properties		Experimental Properties	
Wind Speed	8 m/s		
r/R	0.8		
Relative Velocity	50 m/s	**Relative Velocity**	41 m/s
Blade Chord	1.45 m	**Blade Chord**	0.725 m
Angle of Attack	5.5°	**Angle of Attack**	0°
Re	$4.9x10^6$	**Re (Rotor Stand)**	$2.4x10^6$
		Re (Wind Tunnel)	$1.5x10^6$

Ice Shape Generation

Ice shapes are generated at the Penn State Adverse Environment Rotor Test Stand (AERTS) [23]. The AERTS facility (Figure 3-3) is a 20 ft x 20 ft x 20 ft cold chamber enclosing a 120 Hp rotorstand. The facility can accurately generate a wide range of icing clouds with controllable LWC, MVD, and temperature input. The icing cloud is generated by NASA standard icing nozzles which, aerosolize water droplets with a precise combination of water and air pressure. This is regulated by a feedback control system, which maintains droplet size within 2 μm [23].

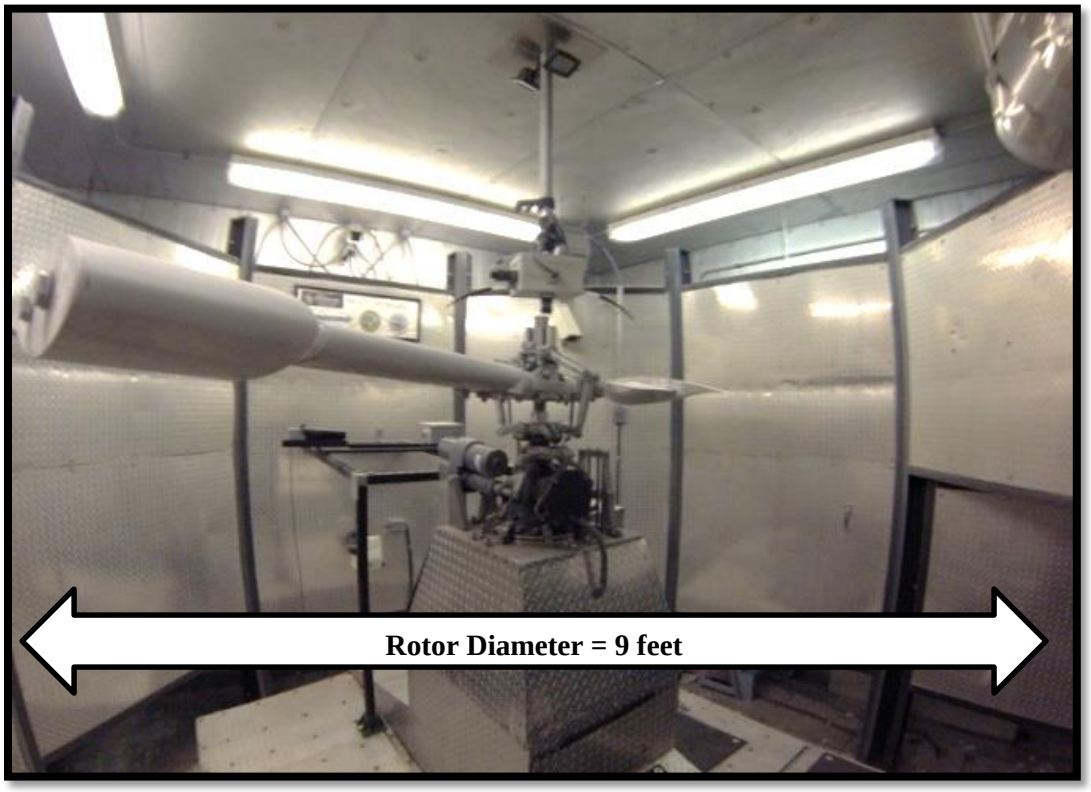

Figure 3-3. Adverse Environment Rotor Test Stand (AERTS at Penn State)

The LWC within the chamber is dependent on rotor-specific flowfield properties and is calibrated using measurements of leading-edge ice thickness in an iterative process for each flow condition. This process yields LWC values accurate to within ± 15% [23]. Icing conditions are scaled based on the change in blade chord with an in-house software, which uses a modified Ruff method [24]. The scaling code is based on a validated NASA scaling method, which evaluates ice accretion by matching collection efficiency, accumulation parameter, and freezing fraction with assumptions that airfoil geometry, flowfield properties, and surface water dynamics remain similar during the scaling [9]. These assumptions are met for the icing conditions and flowfield conditions in Tables 2-2 and 3-1. The scaled icing conditions require lowering MVD and test time to match full-scale conditions (see Table 2-3 for scaled parameters for each case).

LEWICE Validation Testing

Two-Dimensional simulated ice accretions are generated using LEWICE [25] for each freezing fog type ice case in order to compare theoretical full-scale and facility-scale ice accretions. This is a computational validation of the scaling method used and shows how the deficiencies in relative velocity and angle of attack will affect results. A comparison of ice accretions for ice case three in Table 2-3 is displayed in Figure 3-4. LEWICE validation cases are available for all cases in Table 2-3 in Appendix A.

As displayed in Figure 3-4, the facility-scale ice accretions are slightly different from the full-scale ice accretions due to the discrepancy between 0° and 5° angle of attack. The two dimensional area of the ice accretions remains the same, but the shape distribution is changed. The maximum thickness decreases by 14% for the ice accretion at 5° angle of attack and the location of maximum thickness has moved lower on the airfoil. In addition, the ice impingement limits on the upper and lower surface have shifted. However, the surface roughness characteristics of the ice shape are preserved between angles of attack.

The shape change will yield small differences in the airfoil flowfield and resulting aerodynamic performance, but the effect is expected to be that of adding or removing camber to the airfoil and thereby simply shifting the zero-lift angle of attack. This is less significant than the decrease in lift curve slope and increase in drag due to surface roughness impacting the boundary layer development. If a more significant horn shape were present, severe shape differences could cause separation at the leading edge and significantly change the flowfield properties. However, the relatively small changes in shape for these icing scenarios are not expected to cause this severely adverse flowfield behavior.

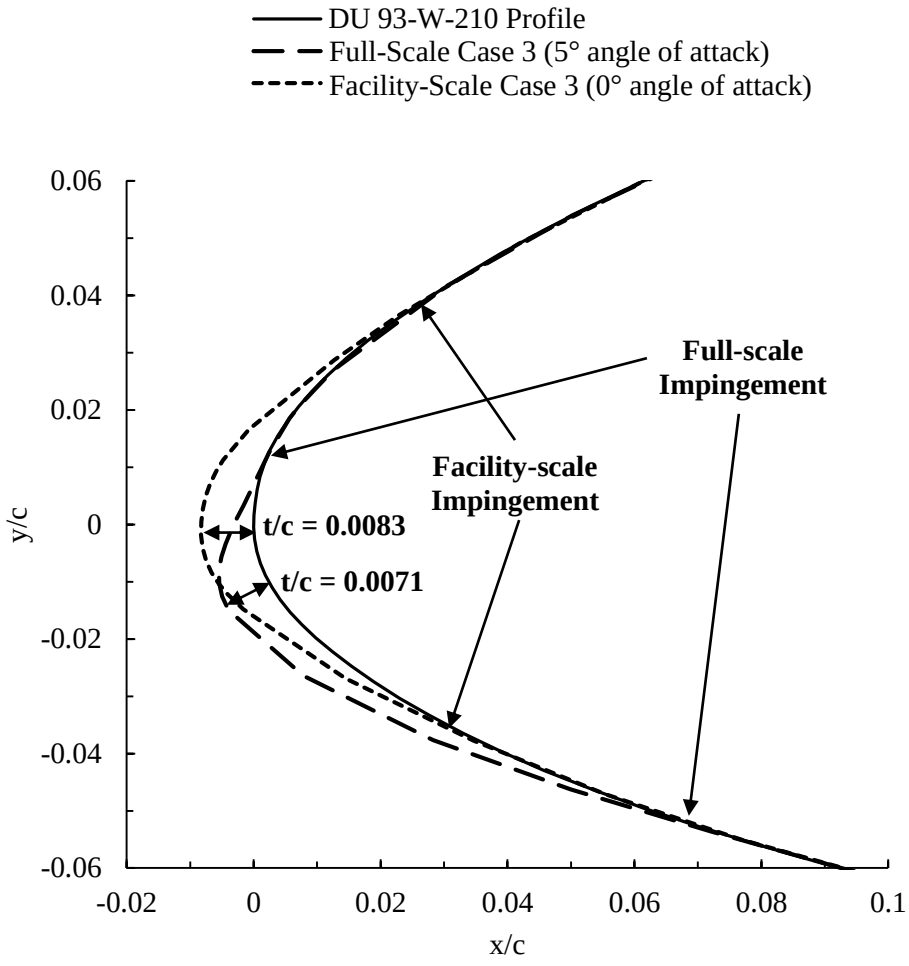

Figure 3-4. LEWICE accretion for Case 3 in Table 2-3.

Ice Accretion Experiments

Ice accretion experiments are performed in the AERTS facility by spinning two blades into an iced flowfield generated by overhead nozzles. A top view schematic of the facility is displayed in Figure 3-5 where dimensions of the DU 93-W-210 blade section and its distance from the rotational axis can be taken from Figure 3-2.

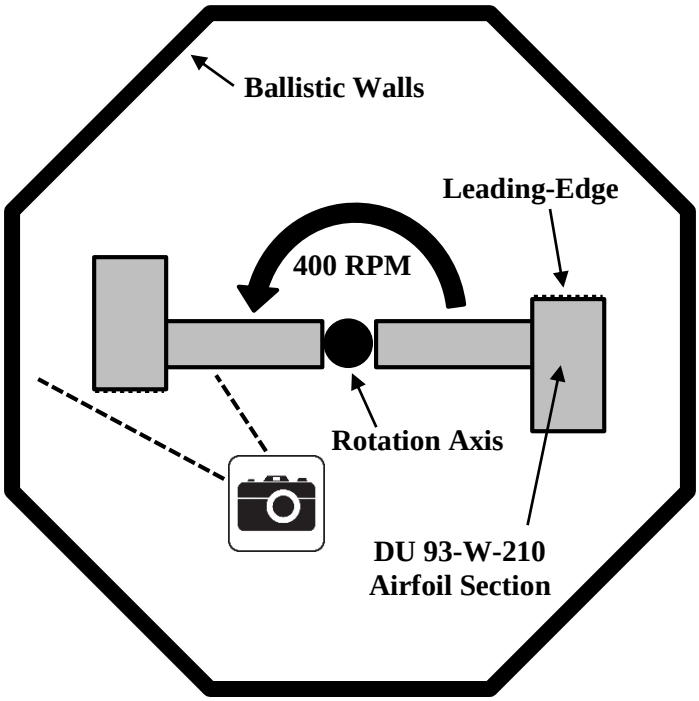

Figure 3-5. Top view schematic of AERTS facility.

Experimentation required operation of the AERTS facility near a limiting boundary. The specific LWC characteristics of the test blade gave a minimum LWC of 0.255 g/m³ using only one of the array of eight overhead nozzles. This low LWC limit is represented by the bottom of the facility envelope in Figure 2-5. The low LWC also introduced a limitation in the minimum droplet diameter achieved in the facility.

The low LWC placed the feedback controller at the lower bound of nozzle calibration curves, which control water and air pressure supplied to the nozzles. If the actual value of water pressure entering the nozzles fell below a certain threshold, the feedback control system was unable to recover and would shut down. Restarting the control system after a shutdown is possible, but this restart method leaves a critical gap of ice accretion time and compromises the integrity of the experiment. The lowest obtainable MVD without system shutdown was determined by iterative

experimentation to be 14 μm. This value determines the left-hand border of the facility envelope in Figure 2-5.

As described in Chapter 2, icing conditions were selected after determining the limitations of the facility and are listed in detail in Table 2-3. A video of an ice accretion test is available in Reference 35. See Appendix D for detailed photographs of casted ice shapes. Some general photographs (see camera icon in Figure 3-5 for location of photograph) of rime ice and glaze ice accreted on the DU 93-W-210 blade section are pictured in Figures 3-6 and 3-7, respectively.

Figure 3-6. Rime Ice - LWC: 0.21 g/m³, MVD: 20μm, T: -21°C, Time: 2 min.

Figure 3-7. Glaze ice - LWC: 0.45 g/m³, MVD: 18μm, T: -3° C, Time: 15 min.

Ice Shape Preservation and Casting

Once an ice shape is generated within the AERTS facility, it is preserved for subsequent wind-tunnel measurements. The delicate ice shapes are molded using a technique developed at the NASA Icing Research Tunnel [26], but modified with the use of high-precision molding and casting materials from Smooth-On, Inc. [18]. The blade section is removed after an icing test and placed into a custom fabricated aluminum molding box (Figure 3-8). The molding box is designed to enclose the blade up to 17.5% of the chord length from the leading edge. The length of the enclosure ensures that the mold captures all ice impingement and is determined by early experimentation and LEWICE accretion results. A silicone rubber molding material is mixed, poured, and cured for 24 hours at a temperature below freezing to preserve detailed ice features. This molding process displayed in Figure 3-9 occurs immediately after running a test to ensure no ice features are lost to sublimation.

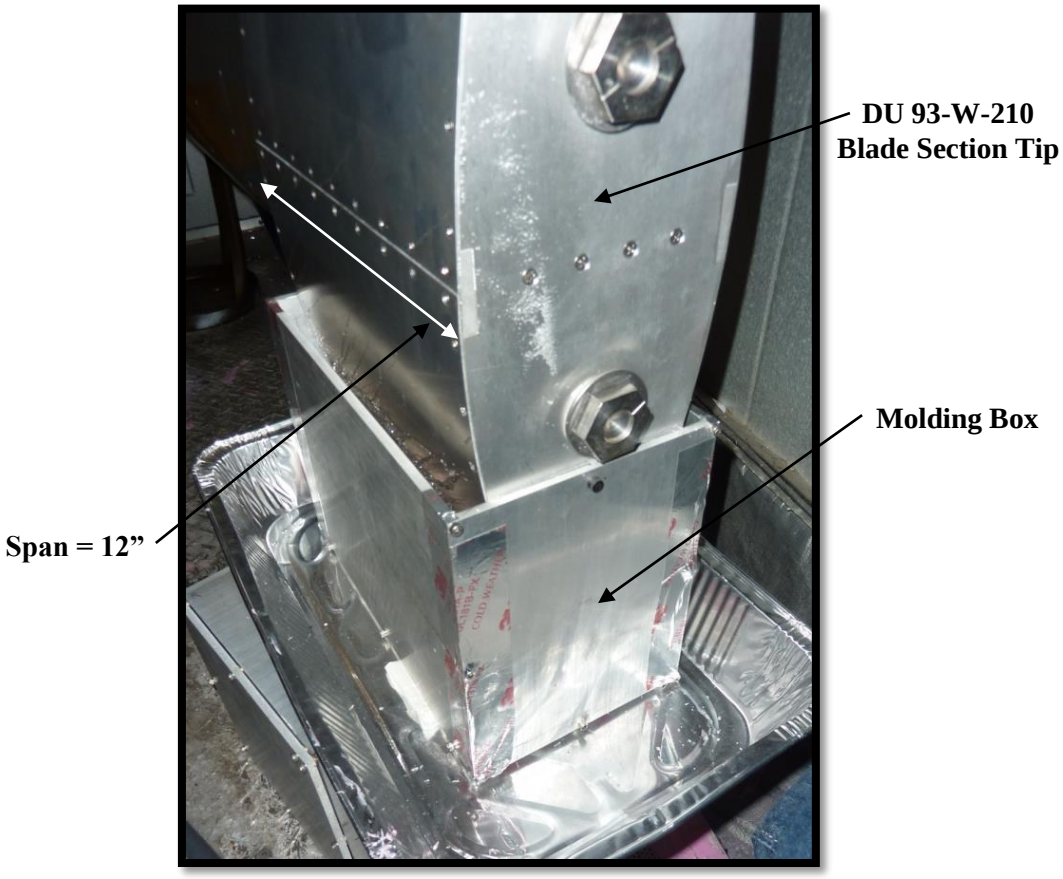

Figure 3-8. Aluminum molding box with DU 93-W-210 airfoil blade section.

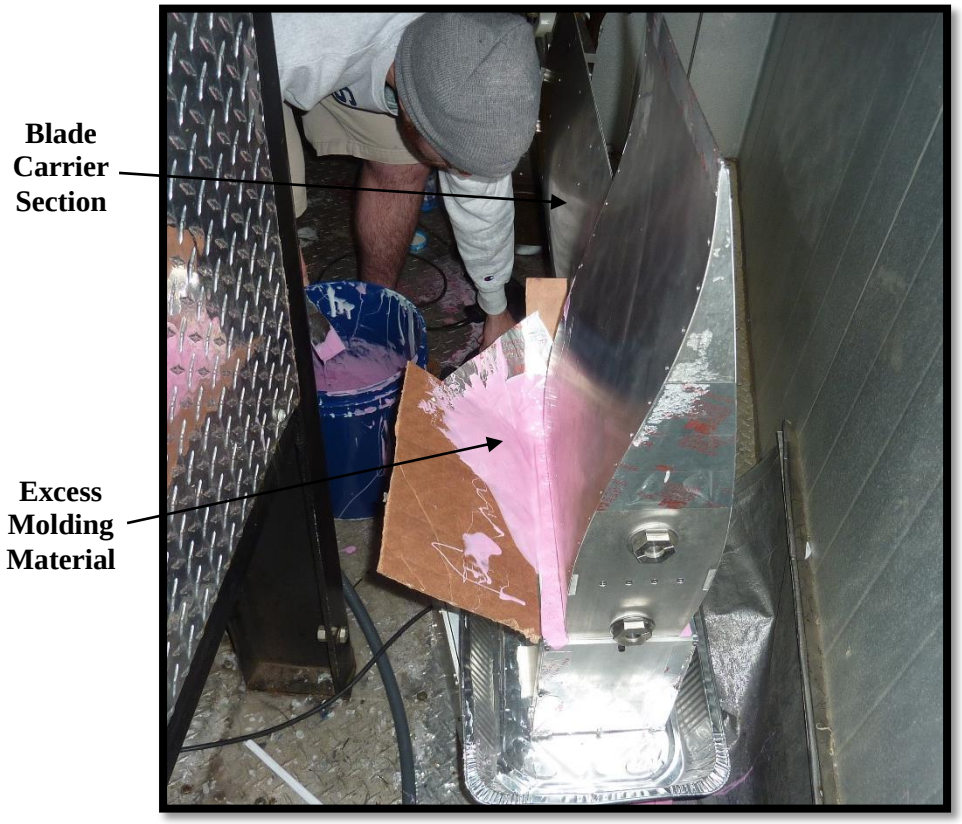

Figure 3-9. Mold pouring at -12° C.

A single mold (Figure 3-10) is taken for each case and employed to make two 12” span epoxy resin castings. Each casting is poured with preplaced mounting bolts that are aligned with a precision machined and custom designed aluminum template (Figure 3-11). The casting material simply fills around the nuts and bolts, anchoring the nuts and creating a precise thread pattern for the bolts. This method creates a high-precision mounting mechanism when the casting is mounted to the wind-tunnel model (see Figure 3-12). Removing the castings from the mold is a difficult process that does remove some material, but the vast majority of surface roughness elements remain.

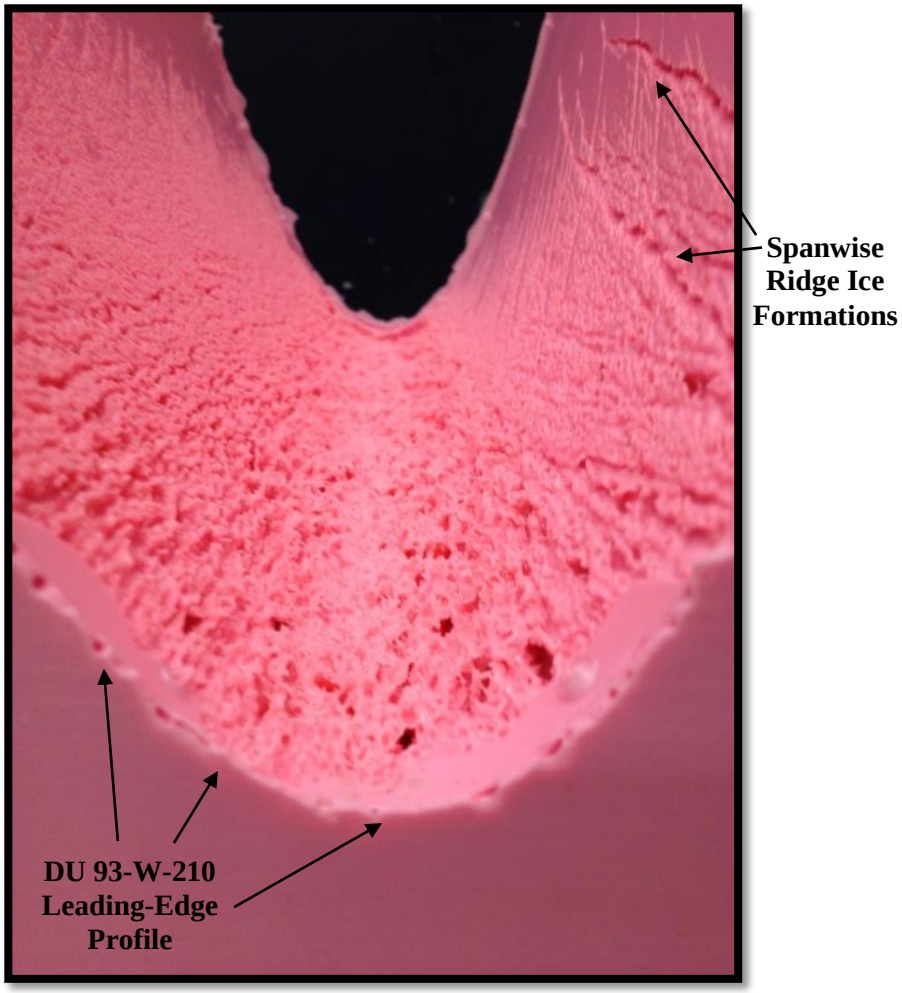

Figure 3-10. DU 93-W-210 blade section: glaze ice mold.

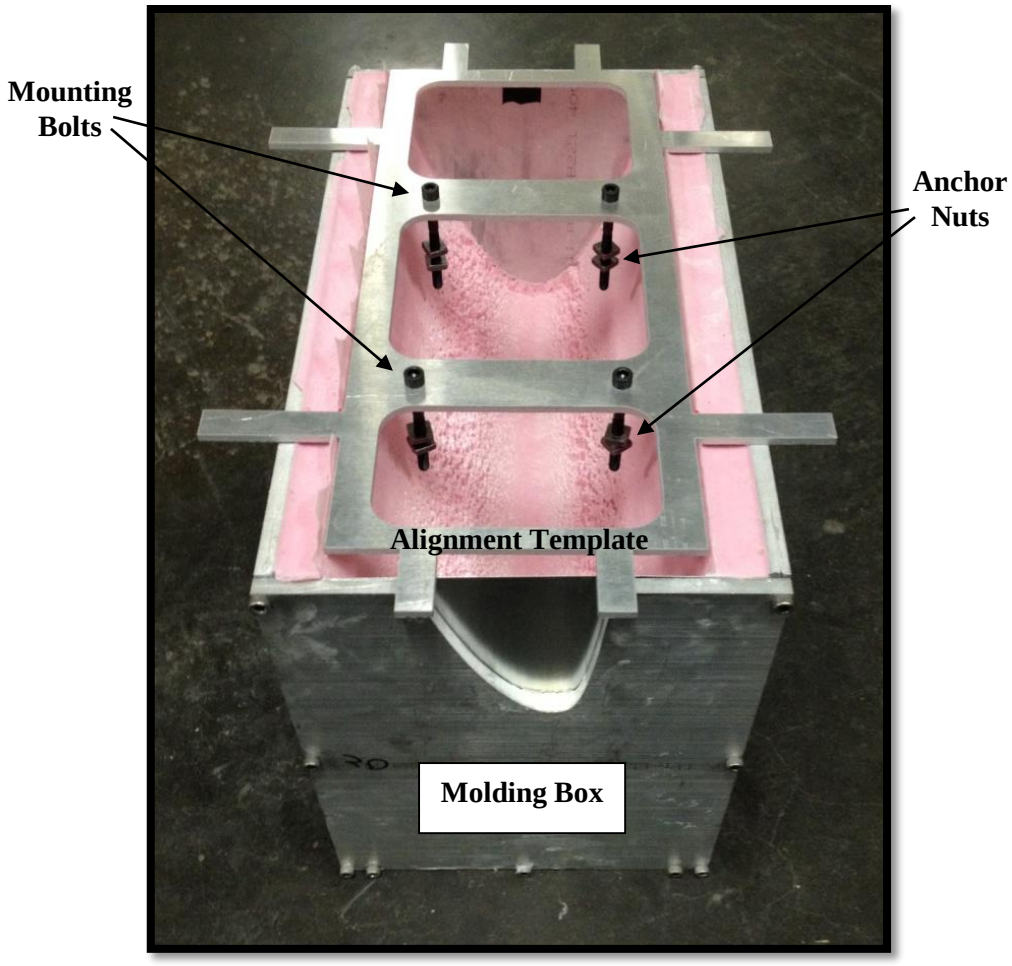

Figure 3-11. Precision template with sunken bolts aligned for a casting.

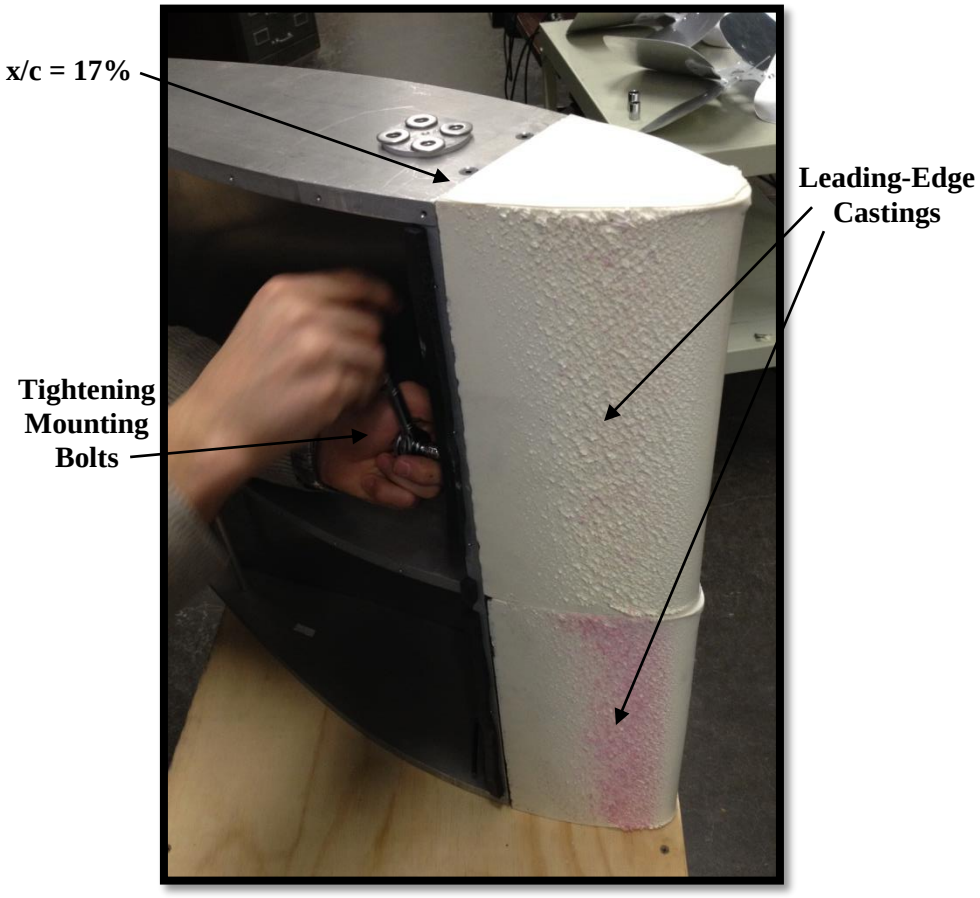

Figure 3-12. Wind-tunnel model with mounted ice shapes.

Special attention is given to each wind tunnel model once a casting has been mounted. The transition from the leading-edge casting to the aluminum wind-tunnel model is critical since a lip or gap could significantly alter the airfoil flowfield and associated airfoil performance. Each model is carefully studied to find lips and/or gaps and eliminate them with either sanding of the model or filling the gap with a pink putty filler material (see Figure 3-13). Although this process is done by hand, careful attention is given to not alter the shape of the airfoil when filling and sanding the model. Some cases hardly need treatment, but others require up to four or five iterations of filling and sanding until a completely smooth transition is ensured.

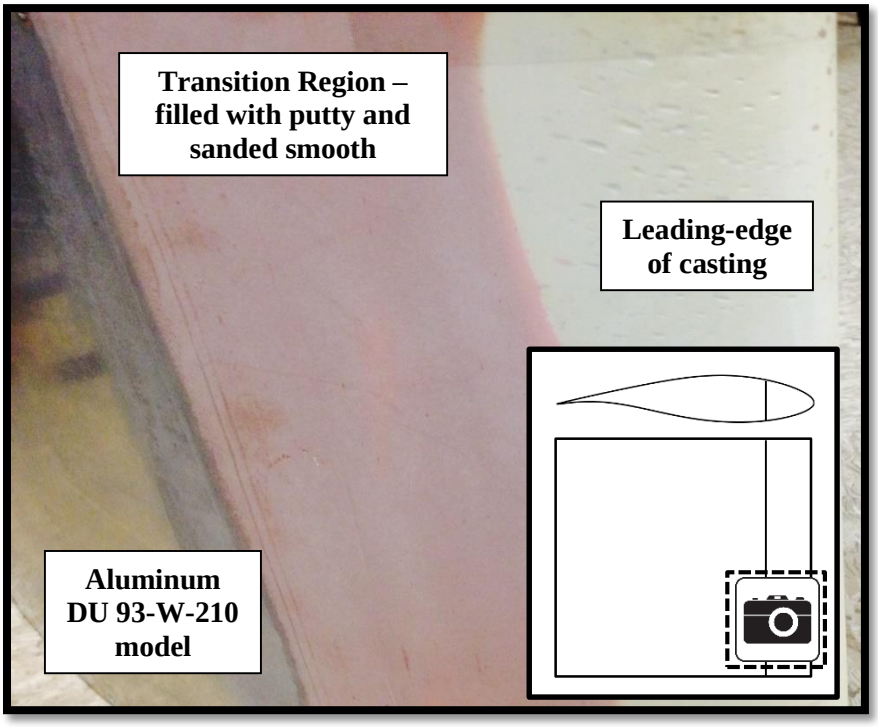

Figure 3-13. View of wind-tunnel model transition region.

The casting resolution (compared to a millimeter scale in Figure 3-14 and a dime in Figure 3-15) captures details as fine as 1/1000th of an inch. This measurement is made by digitally measuring the smallest fully distinguished roughness element in Figure 3-14 and corresponds to a k/c value of 0.00003. The roughness elements vary greatly depending on the icing condition (see Figures D-1 through D-6 in Appendix D) and with k/c values ranging from 0.00003 to 0.0105. These castings capture the true surface roughness of the ice, which is responsible for significant differences in drag penalties between icing cases.

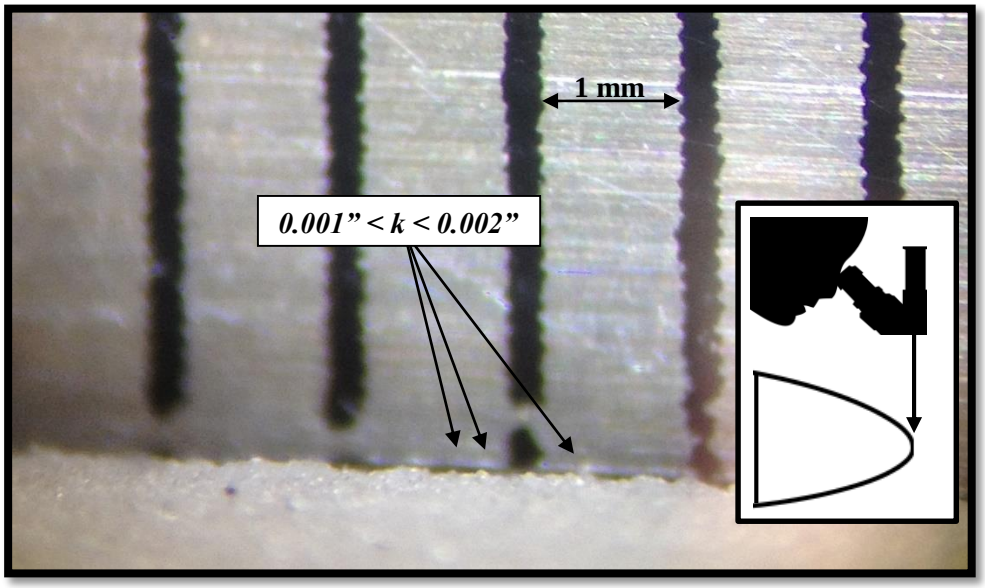

Figure 3-14. Microscope view of leading-edge rime ice compared to a millimeter scale.

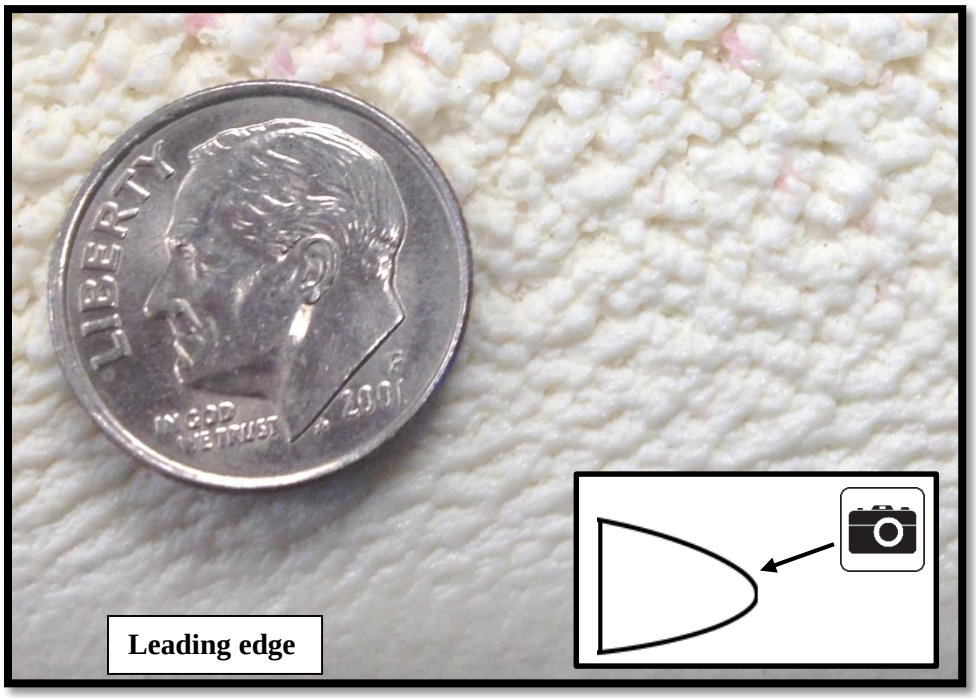

Figure 3-15. Leading-edge ice at the transition from the smooth to rough zones.

Surface Roughness Measurements

Both surface roughness impingement zones and surface roughness heights are measured. The measurement technique depends on the height of the roughness element. Elements in the feather region are typically greater than 0.02” and are measured manually with a set of calipers. Elements in the rough zone (see Figure 4-1) are measured using a dial indicator and a precision milling table. The setup is illustrated in Figure 3-16 and allows for precision measurements within 1/1000th of an inch. Finally, the smallest elements in the rough zone are measured by digitally analyzing photographs of leading edge ice under a microscope (see Figure 3-14). The region impingement lengths are measured by first using a straight edge and a pencil to map out regions as depicted in Figure 4-1 on the casting cross section. Then regions are measured using calipers.

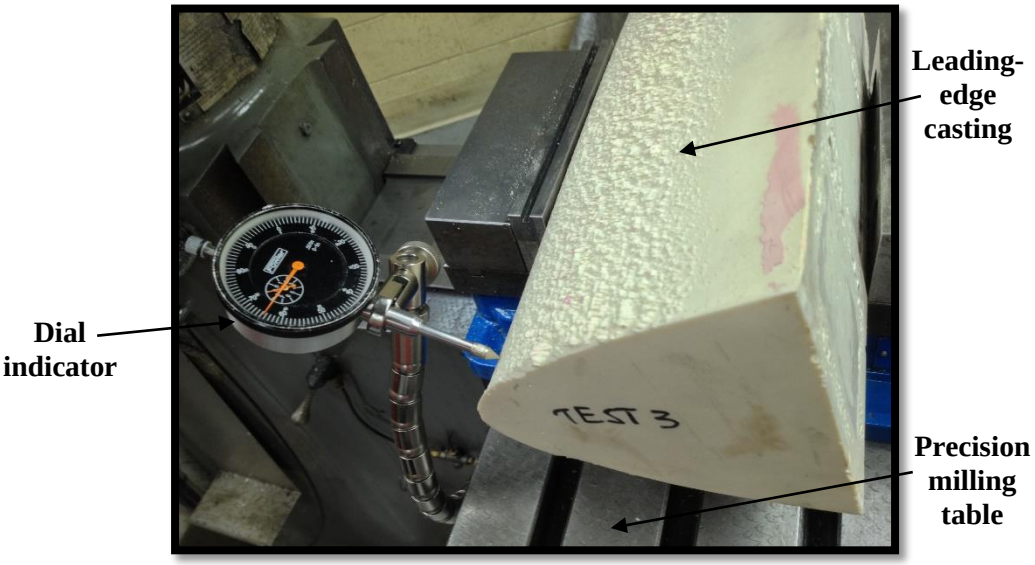

Figure 3-16. Precision measurements of ice surface roughness.

Wind Tunnel Testing

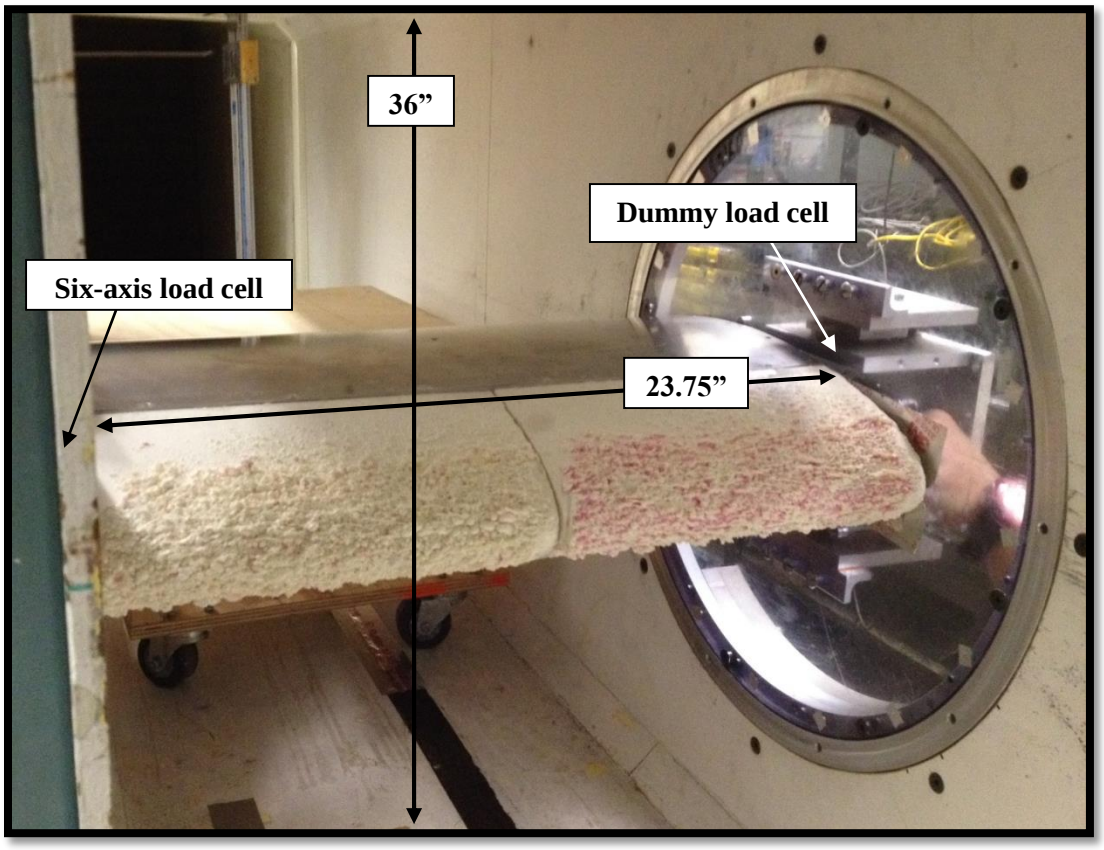

Figure 3-17. DU 93-W-210 airfoil with glaze ice mounted in the wind tunnel.

Measurements of lift and drag are taken at a Reynolds number of 1.5 million in the Hammond low-speed wind tunnel at Penn State. The Hammond tunnel is a single-return closed loop wind-tunnel with a 24” x 36” test section. A pressure differential between the diffuser and test section is used to measure wind-tunnel velocity. Pressure measuring instruments are calibrated prior to testing at a temperature that stayed consistent between calibrations.

The DU 93-W-210 model is mounted horizontally to a six-axis load cell on one wall and a “dummy” load cell on the other wall (see Figure 3-17). The “dummy” load cell has the same size and shape of the load cell without the strain gauges for measuring forces and moments. The model itself has a span of 23.75” to allow for 0.125” gaps between the model and the wind-tunnel walls.

Lift and drag measurements are taken using an axially mounted six-axis load cell in an attempt to capture 3D flow effects that are integrated across the span of the tunnel model. The measurements on the load cell are multiplied by a factor of two to give the total force on the model. This factor assumes that forces are acting at the geometric center of the model. This is a reasonable assumption given the precision of the experimental setup.

The size of the DU 93W-210 airfoil section and associated tunnel blockage requires blockage corrections to load cell measurements. Large blockage has the effect of increasing local velocities over the airfoil surface due to influence of the wall boundary [28]. The model blockage is unfavorably high at 17%, but is unavoidable and a result of trade-offs in designing two experiments, i.e. ice-accretion and wind-tunnel testing, with a common model size. However, valuable work is still possible at blockage values of up to 20% [28] and the measured data sufficiently distinguishes aerodynamic properties between ice cases.

In this work, a blockage correction is performed following the work of Pope [29]. Due to the airfoil camber, the actual blockage in terms of frontal area to tunnel area remains at about 17% throughout the operation from -5° to 7° angle of attack. This allows for the use of one blockage correction that is applied throughout the range of angles of attack. Equation 3-1 shows the blockage parameter, which incorporates an empirical correction factor (K_1), model volume (V_{Model}), and test tunnel sectional area (C).

$$\epsilon_{sb} = (K_1 * V_{Model})/C^{3/2} \quad [3\text{-}1]$$

$$V = V_u(1 + \epsilon_{sb}) \quad [3\text{-}2]$$

$$c_l = 2L/\rho V^2 bc \quad [3\text{-}3]$$

$$c_d = 2D/\rho V^2 bc \quad [3\text{-}4]$$

$$\frac{c_{x,corr}}{c_x} = \frac{1}{(1+\epsilon_{sb})^2} = 0.8925 \quad [3\text{-}5]$$

This results in a corrected velocity used to non-dimensionalize force-balance measurements that is of the form of Equation 3-2 where V is the corrected velocity and V_u is the uncorrected measured wind-tunnel velocity. The velocity difference is carried through non-dimensional coefficient equations for lift and drag (Equations 3-3 and 3-4 respectively) to yield an equation for the difference between corrected and uncorrected non-dimensional parameters (Equation 3-5). This results in an 11.75% reduction in lift and drag coefficients from the original measurement. This is a notable correction because of the large model size.

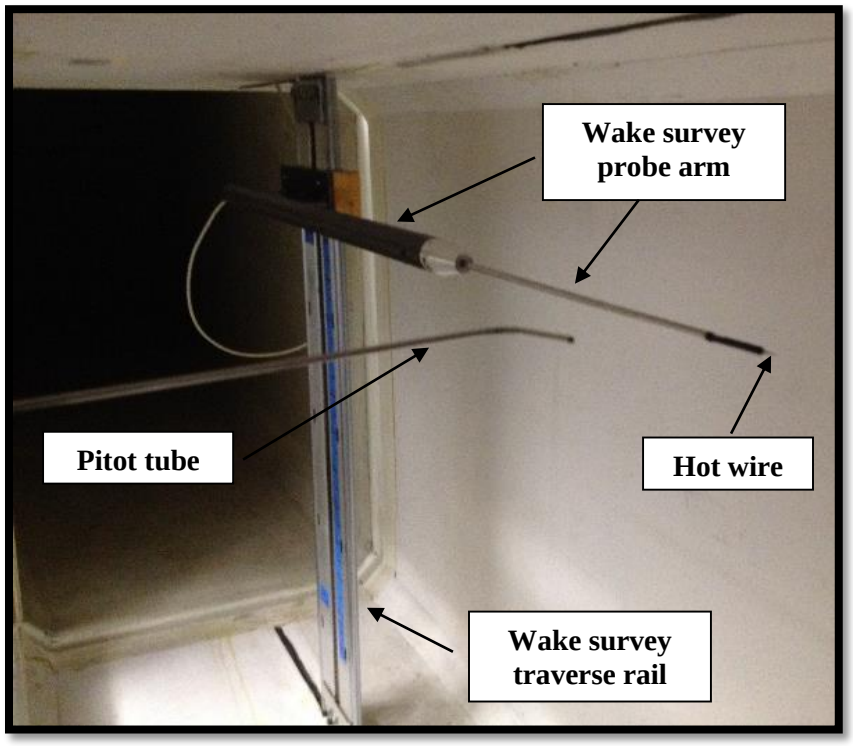

Figure 3-18. Wake survey setup with Pitot tube for calibration.

An additional wake survey measurement is taken to remove increases in load cell measured drag due to wall effects. The wake survey is located 0.7c downstream of the airfoil trailing edge as recommended by Pope [29]. The wake survey measurements are made using a constant temperature hot wire anemometer (see Figure 3-18) with a platinum hot-film measuring 50.8 μm at an over-

heat ratio of 1.6. The hot wire is first calibrated using measurements of velocity of a nearby pitot tube compared to voltage on the wire. This calibration step yields a fourth-order polynomial curve fit for measuring velocity and turbulence intensities. The actual drag measurement is made by integrating velocity deficits in the wake region compared to the "freestream" velocity measured by the wake probe. One would expect a straight line when taking the freestream measurement, but the line is slanted as displayed in Figure 3-19.

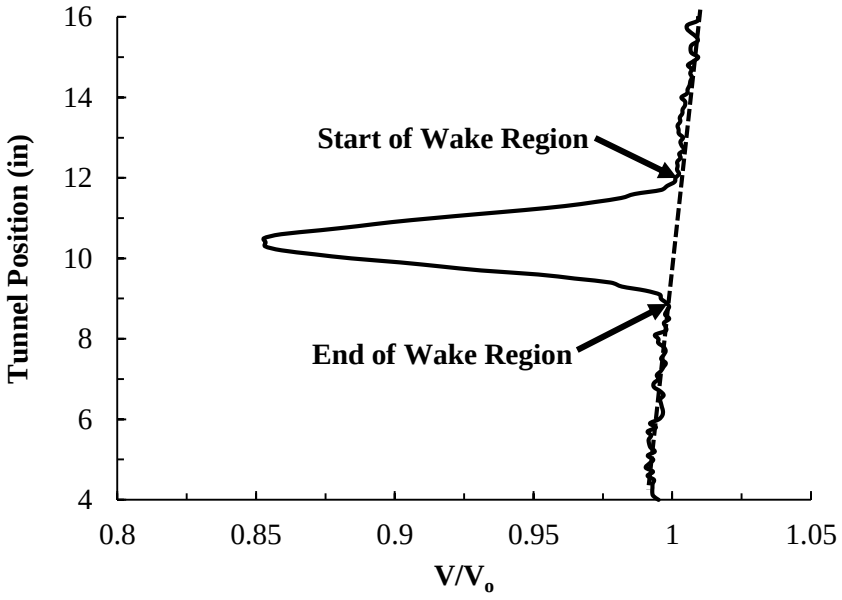

Figure 3-19. Wake Survey Measurement at 4° Angle of Attack

The slant in the line is due to heating of the wind tunnel airflow during the 15 minute wake survey traverse. The warmer air very slightly lowers the voltage required to heat the constant temperature wire, which results in a lower velocity measurement than expected. However, the error in actual velocity measurement is insignificant due to the fact that drag measurements are based on a velocity deficit, which is practically unchanged even in a heated air stream. Equation 3-6 gives the drag coefficient calculation based on the measured velocity deficit and is a result of basic momentum theory [29]. Blockage corrections are not made to the wake measurements.

$$c_d = \frac{2}{c}\int \frac{V}{V_0} - (\frac{V}{V_0})^2\, dy \qquad [3\text{-}6]$$

The term V_0 represents the freestream velocity measurement, but is modified to be the average of the freestream measurements made by the hot wire anemometer at the start and end of the wake region (see Figure 3-19). Wake survey measurements are used to make a correction to load cell data, which is described later in this chapter.

Wind-Tunnel Validation Testing

An effort is made in this research to ensure that wind tunnel measurements are as accurate and accountable as possible. The wind-tunnel data are of highest importance because they dictate aerodynamic penalties, which are the basis of conclusions of this research. The first part of the validation effort is to test an S805 airfoil before making measurements for the DU 93-W-210 blade profiles. This is done to compare the measurements to known published data and validate the lift and drag measurement system.

The lift measurements taken by the horizontally mounted load cell match very well against published data [27]. There is a small discrepancy between 1° and 9° angle of attack where the reference data are slightly above the load cell data (see Figure 3-20), but the load cell measured data follow a linear pattern. This decrease in lift measurement could be due to increased roughness of the model used and increased turbulence in the wind-tunnel compared to the reference data. However, the linear trend of the measured data follows analytic predictions and matches within 10% of the published comparison.

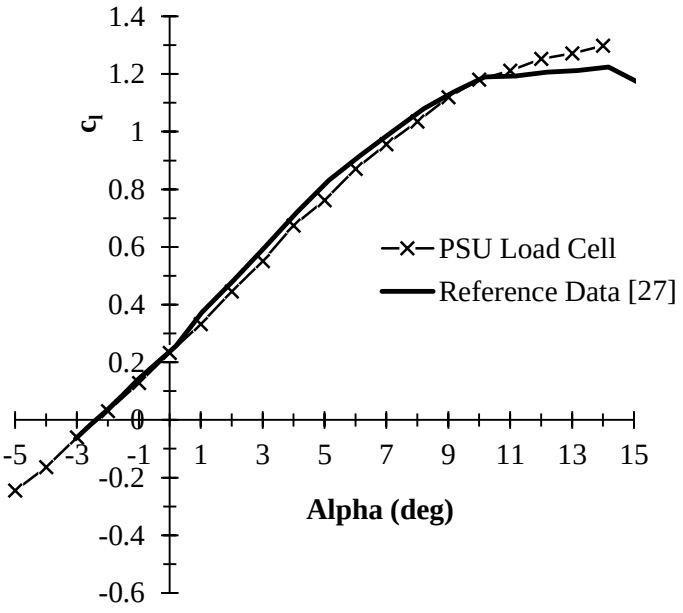

Figure 3-20. Validation of lift measurements for an S-805 airfoil [27].

There is a discrepancy near stall in which the load cell measured lift continues to rise while the published lift curve begins to stall. This is most likely due to blockage within the Hammond wind tunnel delaying stall on the model. Although this trait is undesired for testing the DU 93-W-210 airfoil, it is of less significance since power predictions will be mainly driven by integration of aerodynamic loads below the stall range of angles of attack. The load cell system for measuring lift is therefore considered to be validated for use on the DU 93-W-210 airfoil sections.

The measurement of airfoil drag is even more important than lift due to the sensitivity of airfoil drag to icing roughness and the leading impact on wind turbine torque. In addition, the drag force is much smaller than the lift force and is therefore more difficult to accurately measure with the use of a load cell. The load cell drag measurements displayed in Figure 3-21 match well near the location of zero lift, but are increased at higher and lower lift measurements. This discrepancy at high angles of attack is due to flowfield interaction at the gaps between the model and wind tunnel walls. However, the wake survey measurements displayed in Figure 3-21 match well with

the published data throughout the entire angle of attack range. The discrepancy seen in the load cell measurements has vanished since the wake survey is measuring drag only using flowfield measurements from the center of the wind tunnel, omitting the unwanted wall interactions. This conclusion leads to the use of a correction to load cell data using the wake survey measurements and is described in more detail in the next section.

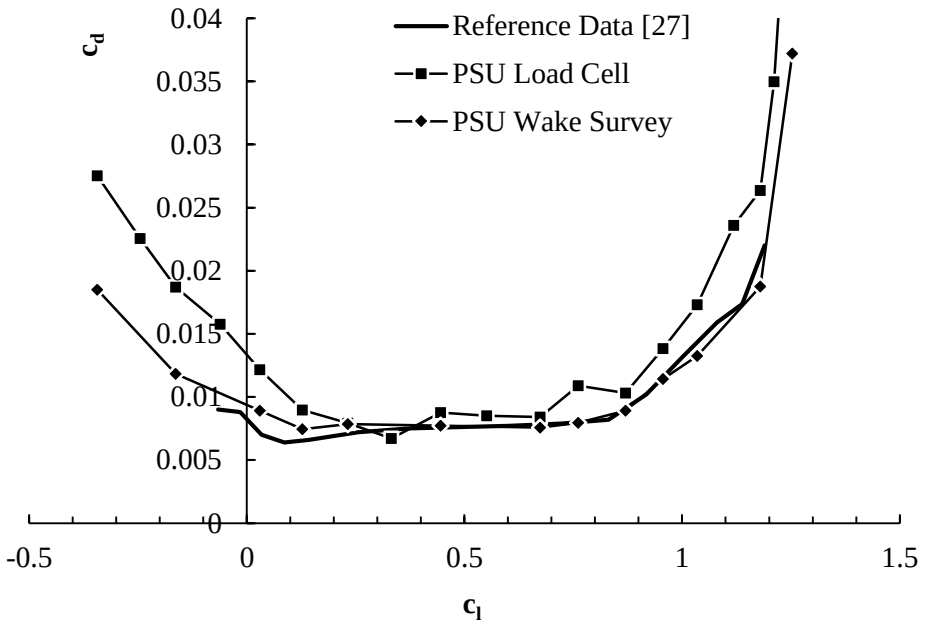

Figure 3-21. Comparison of drag measurements for an S-805 airfoil.

Once the lift and drag measurements using the load cell were validated using the S-805 airfoil, measurements on the clean DU 93-W-210 model are made. The measurements are displayed in comparison to measurements made by T.U. Delft in Figure 3-22. There is a clear discrepancy between the clean lift curves, but the PSU measurements match almost exactly with Delft measurements of a tripped boundary-layer case. Although undesired, the reason that the Hammond wind-tunnel model is behaving as though the flow is tripped is easily justified. The leading-edge

casting roughness, sensitivity in the casting to model transition region, and increased turbulence in the Hammond wind-tunnel are all likely contributors to forcing early transition on the model.

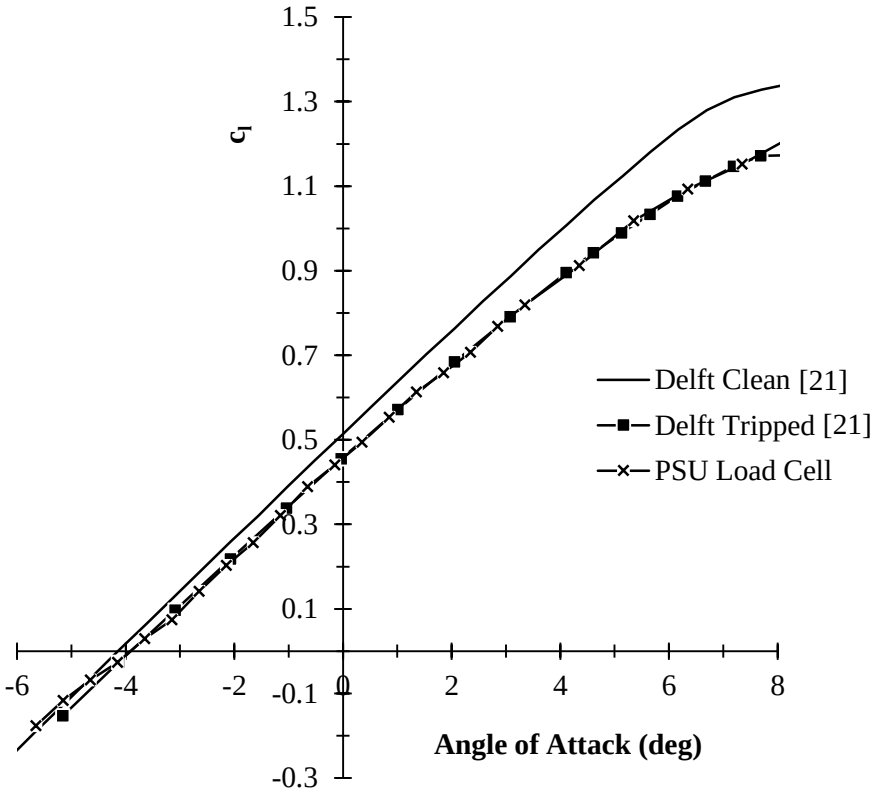

Figure 3-22. Comparison of lift measurements for the clean DU 93-W-210 airfoil.

The initial load cell drag measurements for the clean DU 93-W-210 airfoil are less successful than for the lift. The sensitivity of the measurement of small forces has an effect on the accuracy of the drag coefficient measurements, which is easily illustrated by the large deviations of the drag curve in Figure 3-23. The issue of drag increase at high lift due to wall interactions is quite large for the DU 93-W-210 airfoil. Drag at high lift is more than 100% higher than Delft measurements. The drag for all ice cases is measured using the load cell setup, but is then corrected later after taking wake survey measurements as described in the next section.

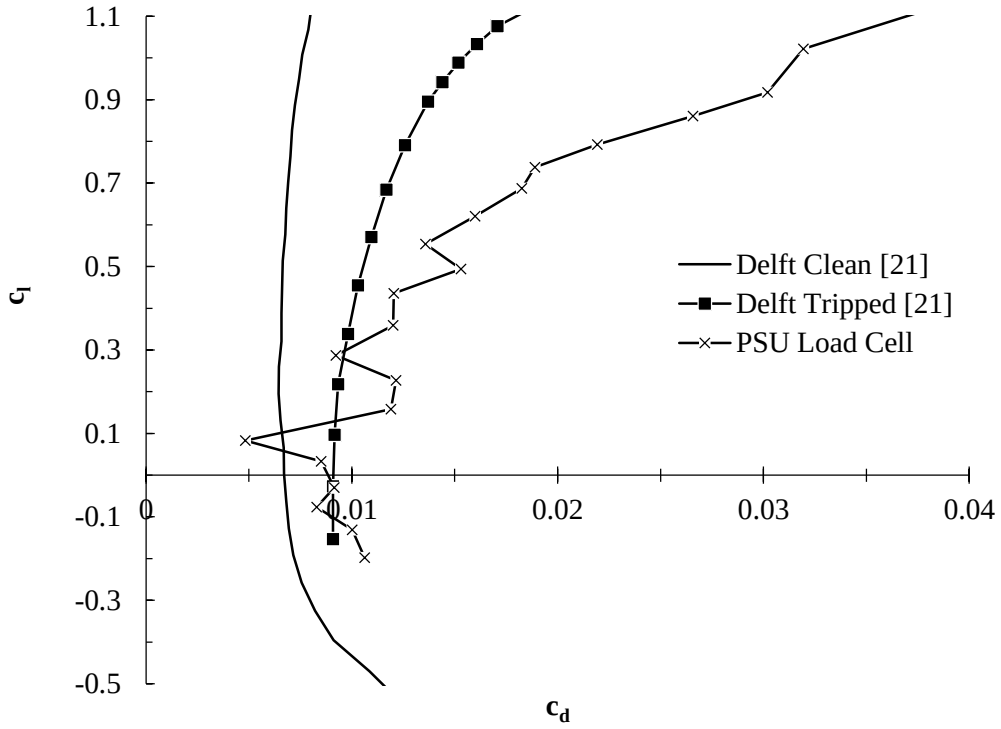

Figure 3-23. Comparison of load cell drag measurements for the clean DU 93-W-210 airfoil.

One important issue discovered in measuring drag with the load cell was the sensitivity of the model mounting to the measured data. The model mounting was so sensitive, that even loosening or tightening a single bolt on the model could affect the results of a test. After extensive troubleshooting, it was found that the model was not sufficiently constrained to the far wall. The model is mounted on a slider at the far side and is able to shift position on the slider during a test. If the position is shifted only slightly, drag measurements would be inconsistent. Fortunately, this problem was identified by observing that the load cell generates a non-zero drag value when the tunnel velocity was brought to rest. It is worth noting that this problem is only an issue in the drag direction and not the lift direction, most likely due to the construction of the slider. The solution to the problem was to secure the model with clamps on the far wall so that it could not move at all on

the slider. Once secured, drag measurements were consistent, but still require corrections for the influence of the tunnel walls as discussed in the next section.

Wake Survey Correction Method

In hindsight, wake survey measurements should have been solely used for drag measurement since the wall boundary had such a large influence on load cell measured drag. However, the wake survey experimental setup was finished at a later stage in the research timeline and only allowed the testing of the S805 airfoil, the clean DU-93-W-210 airfoil, and one iced DU-93-W-210 airfoil. Therefore, a method to use the measured wake survey data to remove the influence of the wall boundary on measured load cell drag was developed.

Measurements of both the clean and iced DU-93-W-210 airfoil are recorded from the wake survey and load cell. The iced airfoil is case 3 (-10° C) from Table 2-3, which is chosen because it represents the midrange temperatures of the six ice cases. A clear trend exists in the difference between the load cell and wake survey measurements. The difference between these measurements is plotted versus angle of attack in Figure 3-24 for both the clean and one iced case. The difference in measured drag coefficients matches almost exactly, confirming that the increase in drag measured by the load cell is due to the wall interactions rather than the flowfield over the wind-tunnel model. This similar correlation between the two separate flowfields also justifies the use of a correction factor generated from one data set that can be applied for all other cases.

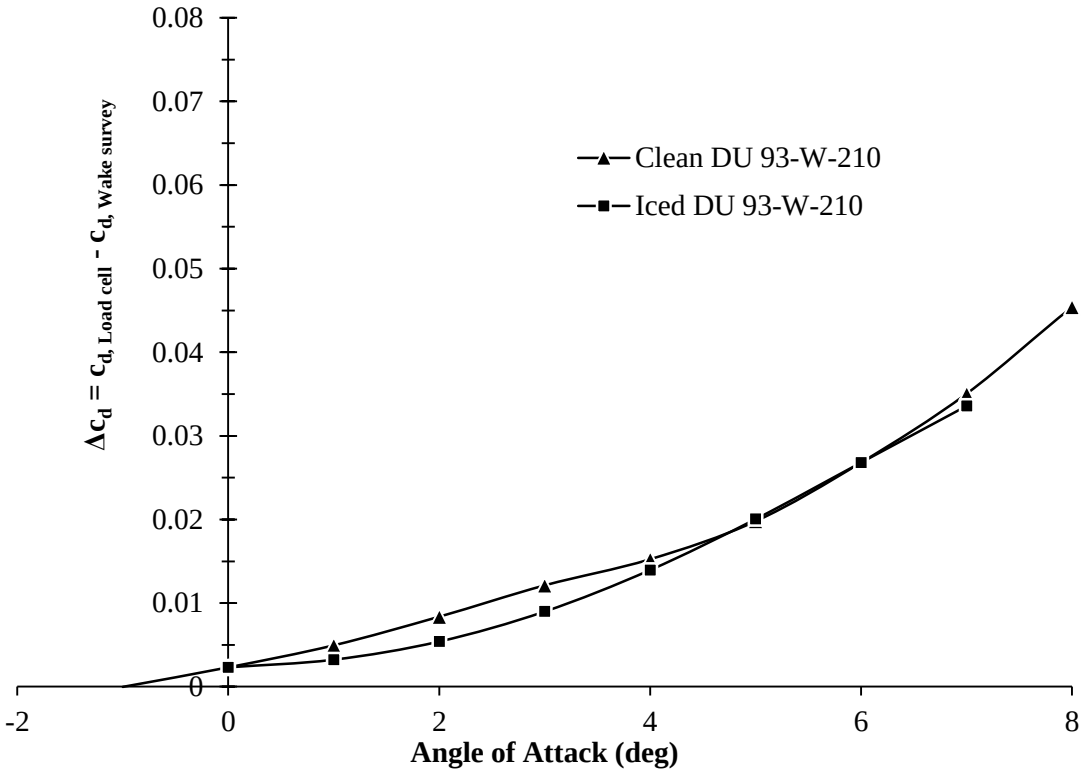

Figure 3-24. Drag difference between load cell and wake survey measurements.

In order to best capture iced airfoil data, the difference from Figure 3-24 is used to create the correction factor. The correction factor is simply a second-order curve fit of the drag coefficient difference vs. angle of attack, which is applied only for the angle of attack range in which the wall effects appear to be most severe. Angle of attack is used to create the correction factor because plotting the difference versus lift coefficient revealed a curve fit with a lower r-squared value and required a higher-order polynomial fit, whereas plotting versus angle of attack showed a clear second-order trend. Equation 3-7 gives the correction factor and Equation 3-8 exemplifies how the load cell measured data are treated where Δc_d is the increase in drag coefficient due to wall effects, $c_{d,lc}$ is the drag coefficient measured by the load cell, and $c_{d,new}$ is the new drag coefficient after the wall correction is applied.

$$\Delta c_d = 0.00053719\alpha^2 + 0.00082927\alpha \quad [3\text{-}7]$$

$$c_{d,new} = c_{d,lc} - \Delta c_d \quad \text{for } 0° \leq \alpha \leq 7° \quad [3\text{-}8]$$

This correction factor is applied to all ice cases and is the final step to generate polars for iced airfoils. The tabulated airfoil performance data can now be used as an input to a wind turbine analysis tool to predict power output.

Performance Prediction Using XTurb-PSU

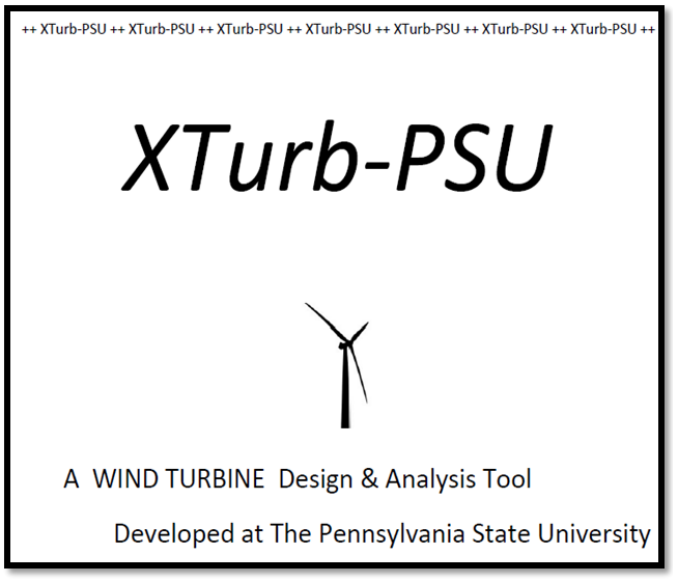

Figure 3-25. XTurb-PSU cover page.

The final step in determining the power losses associated with the icing conditions that have been replicated and wind tunnel tested is to computationally predict wind turbine power. Power is calculated with an in-house wind turbine design and analysis code: XTurb-PSU [30]. XTurb-PSU calculates power using Blade-Element Momentum Theory (BEMT) based on NREL's AeroDyn [31] code and employs a stall delay model by Du and Selig [32] based on NREL's AirfoilPrep worksheet [33].

The XTurb-PSU code (Figure 3-25) is used to provide wind turbine power vs. wind speed as well as any other aerodynamic loading parameters relevant to the BEMT calculations. The code uses an input file, which calls airfoil polar files listed in the blade geometry section of the input file. Analyzing different icing conditions simply requires updating the airfoil polar files to represent the wind-tunnel data measured for that specific icing condition. However, iced airfoil input files required some extrapolation since measured data are only available up to 7° angle of attack.

The lifting properties for each iced airfoil in the stall region are modeled following the lifting properties of the "tripped flow" DU 93-W-210 airfoil measured by T.U. Delft [21]. Stall delay is a property observed for iced airfoils [13], therefore the modification of the lift curve is carried out to give a stall-delay effect. Beyond airfoil stall, XTurb-PSU modifies airfoil data using the Viterna correction to create data from -180° to 180° angle of attack. Drag is easier to model post-stall since the drag is already very high. The drag is simply modified to follow an increase similar to the Delft tripped model [21]. The modified airfoil data for ice case 4 are displayed in Figure 3-26 along with the actual measured data of the tripped Delft Airfoil. The tailoring of the data ensures a smooth transition into realistic values of lift and drag given prior aerodynamic knowledge.

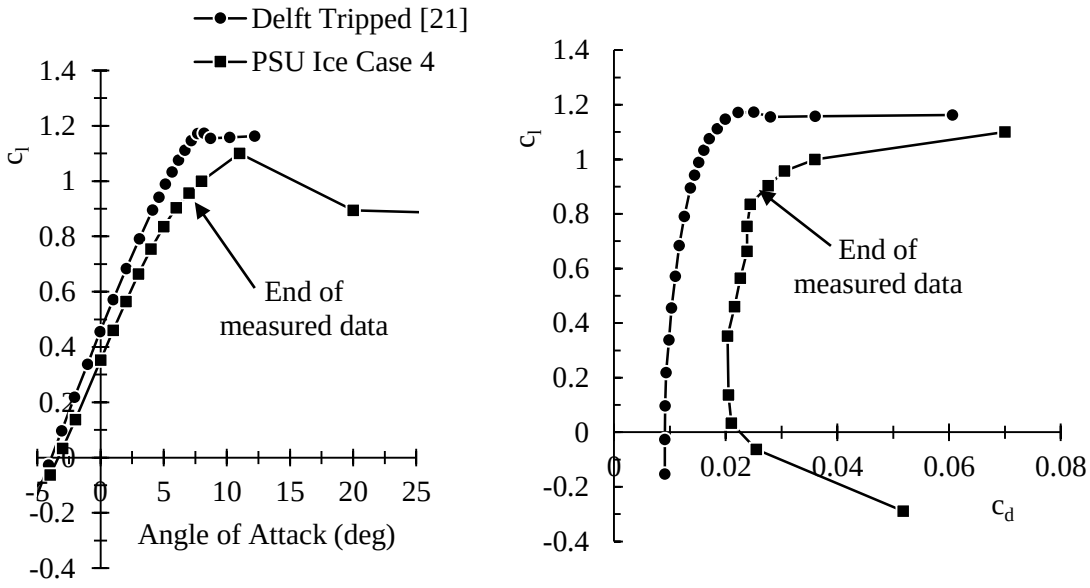

Figure 3-26. Lift and drag comparisons for modified XTurb-PSU airfoil input data.

This method may seem approximate, but less so if one considers the application of the lift and drag information in XTurb-PSU. The angle of attack distribution along the blade span at an average wind speed of 8 m/s is displayed in Figure 3-27. It is clear that within the torque generating span range (refer to Figure 2-3 for review), the angle of attack range is within the measured data envelope or very close to it. The section of the blade operating outside of the measured data region is inboard of the 40% span location and is therefore only weakly affected by the iced airfoil input. It was mentioned previously that the PSU-Ice 1.5MW wind turbine is designed in this way so that measured data are used as accurately as possible.

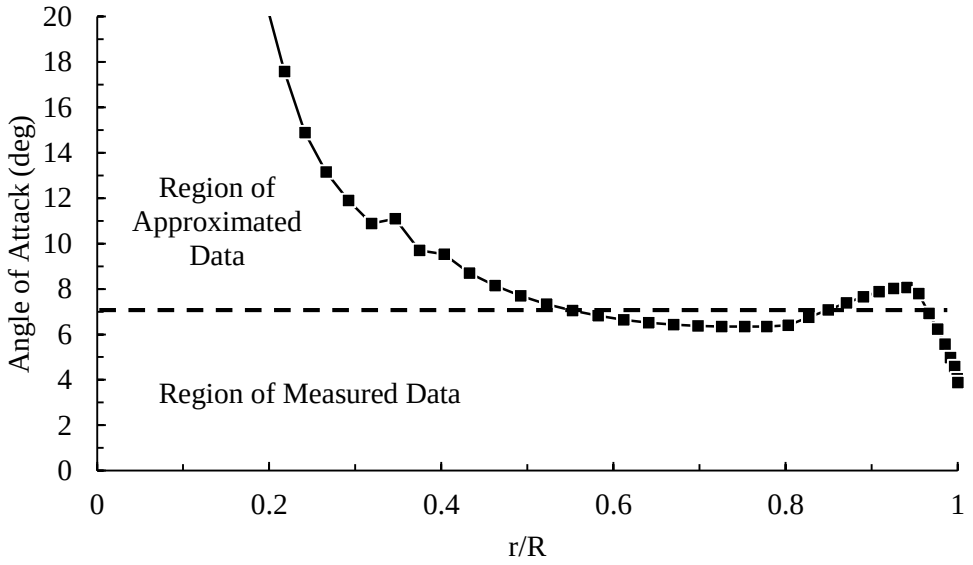

Figure 3-27. PSU-Ice 1.5MW angle of attack distribution at a wind speed of 8 m/s.

The execution of the XTurb-PSU code (for a sweep of 24 wind speeds) takes less than 5 seconds on a laptop computer. Input files for the XTurb-PSU code are available in Appendix C. The results from XTurb-PSU in conjunction with wind-tunnel and ice accretion experimental data are presented in the next chapter.

Chapter 4

Results and Discussion

Three studies are performed, which each yield results leading to the prediction of wind turbine power loss for a utility-scale wind turbine. These studies are ice accretion tests, wind-tunnel tests, and performance predictions using XTurb-PSU. This chapter will give detailed and concise results from these studies whose implications will be discussed after results are presented.

Ice Accretion Tests

Ice profiles have been generated, molded, and casted for six separate icing conditions. Photos of ice accretion tests and individual castings are available in Appendix D. The ice accretion profiles extend between x/c = 0.085 and x/c = 0.175 with a minimum and maximum chord-normalized leading-edge thickness of 0.004 and 0.016, respectively. The ice accretion shape and surface roughness characteristics are typical of the diagram illustrated in Figure 4-1. The ice closest to the leading edge accretes in a smooth layer, but quickly transitions to a rough layer moving away from the leading edge on the upper and lower surfaces. The chordwise characteristics of the ice accretions after the smooth zone are highly dependent on the ice accretion temperature and other icing parameters.

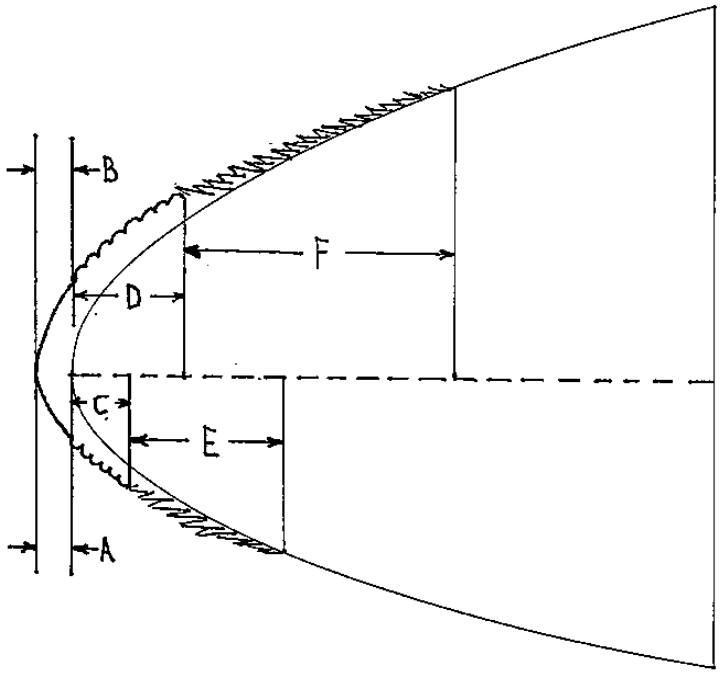

Figure 4-1. Icing zone diagram. See Table 4-1 for descriptions of zones.

Table 4-1. Zone Descriptions for Figure 4-1.

Zone Letter	Description (Surface roughness height range)
A	Leading-edge ice thickness.
B	Smooth zone for the upper and lower surface ($k/c \approx 0$).
C	Lower surface rough zone ($0.00003 < k/c < 0.00039$).
D	Upper surface rough zone ($0.00003 < k/c < 0.00039$).
E	Lower surface feather region ($0.0007 < k/c < 0.0105$).
F	Upper surface feather region ($0.0007 < k/c < 0.0105$).

For warm icing conditions (cases 4 and 5), the smooth layer is either non-existent or immediately followed by a severely rough layer, which quickly blends into a feather region. The feather region extends along the chord until the termination of the ice accretion. Roughness

elements due to splashing, chordwise run-back, and spanwise ridges are also observed on glaze ice profiles (see Figures D-4 and D-5 in Appendix D). The spanwise ridge-ice features are existent because of centrifugal forces on the rotating blade used for ice accretion experiments. Capturing the spanwise ridge ice is important because it can have severe aerodynamic effects [19].

Medium temperature (-10° C) icing conditions (cases 2 and 3) have small smooth and rough zones, which are immediately followed by a feather region. Small ice "feathers" protrude into the direction of the oncoming flow. These feathers are very non-uniform and uncharacteristic in shape (see Figure 4-2), which can cause severe aerodynamic drag penalties. For both the medium and warm temperature icing cases, the ice accretes further along the upper surface than the lower surface.

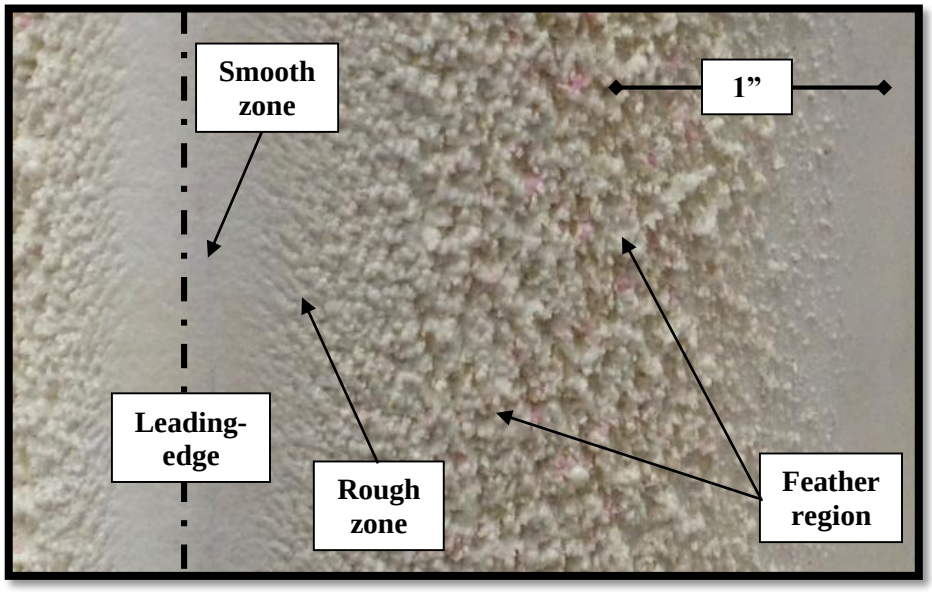

Figure 4-2. Photo of icing roughness.

The very low-temperature rime icing condition (case 1) transitions from a smooth zone to a very slightly rough layer, which extends all the way to the ice impingement limit. The ice accretion from this case is the only one in which the lower surface ice accretes further than the upper surface ice. However, this was also the only case that was run at an angle of attack of 5°

instead of 0°. The leading-edge ice accretion of this very low LWC case is extremely small and hardly changes the shape of the DU 93-W-210 airfoil.

The SLD ice accretion case is characterized by a large leading-edge thickness with ice extending very far back along the chord. Ice extends to roughly 10% of the chord length on the lower surface and 17.5% of the chord length on the upper surface (the entire casting length). The far impingement of the ice is due to splashing of the large droplets and the fact that the droplets have more momentum and can travel further into the boundary layer without being carried away by the outer flow region. This property of SLD ice will have a dramatic effect on airfoil performance, which is described in the next section.

Detailed measurements of ice accretion zones in reference to Figure 4-1 are listed for each icing case in Table 4-2. These zones are important to define since they can be used to aid the generation of simulated iced airfoils for other iced wind turbine performance prediction solvers.

Table 4-2. Ice Dimensions normalized by the chord length.

Case (Table 2-3)	**Zone (Figure 4-1 and Table 4-2)**					
	A	**B**	**C**	**D**	**E**	**F**
Case 1	0.0037	0.0044	0.1096	0.0811	N/A	N/A
Case 2	0.0095	0.0033	0.0044	0.0066	0.0526	0.0965
Case 3	0.0117	0.0044	0.0033	0.0088	0.0767	0.1009
Case 4	0.0109	0.0022	0.022	0.0044	0.0350	0.1009
Case 5	0.0160	N/A	0.0132	0.0175	0.0350	0.0833
Case 6	0.0127	0.0011	0.0088	0.0110	0.0921	0.1754

Wind Tunnel Tests

Lift and drag are measured for each ice case using a load cell with drag increases due to wall effects removed with an empirical correlation based on wake survey drag data (refer to Equations 3-7 and 3-8). Results for lift coefficient vs. angle of attack measurements displayed in Figure 4-3 compare the DU 93-W-210 “clean” airfoil to the six cases referenced in Table 2-3.

The measured test points show a reduction in lift that increases up to 16% with increasing angle of attack. The ice has also effectively de-cambered the airfoil, shifting the zero-lift angle of attack forward by roughly half a degree. The decrease in lift is most likely caused by a separation bubble located near the leading edge. This separation bubble causes a change in the leading-edge pressure distribution and has the potential to alter the stall type of the airfoil [19]. However, the changes in ice roughness do not significantly alter the separation bubble, which results in a similar decrease in lift coefficient across all six ice cases. The only exception is the SLD case, which exhibits particularly poor performance, but also has the furthest impingement of ice along the chord. The sizeable reduction in lift for all ice cases is expected to dramatically lower the torque produced by iced blade sections.

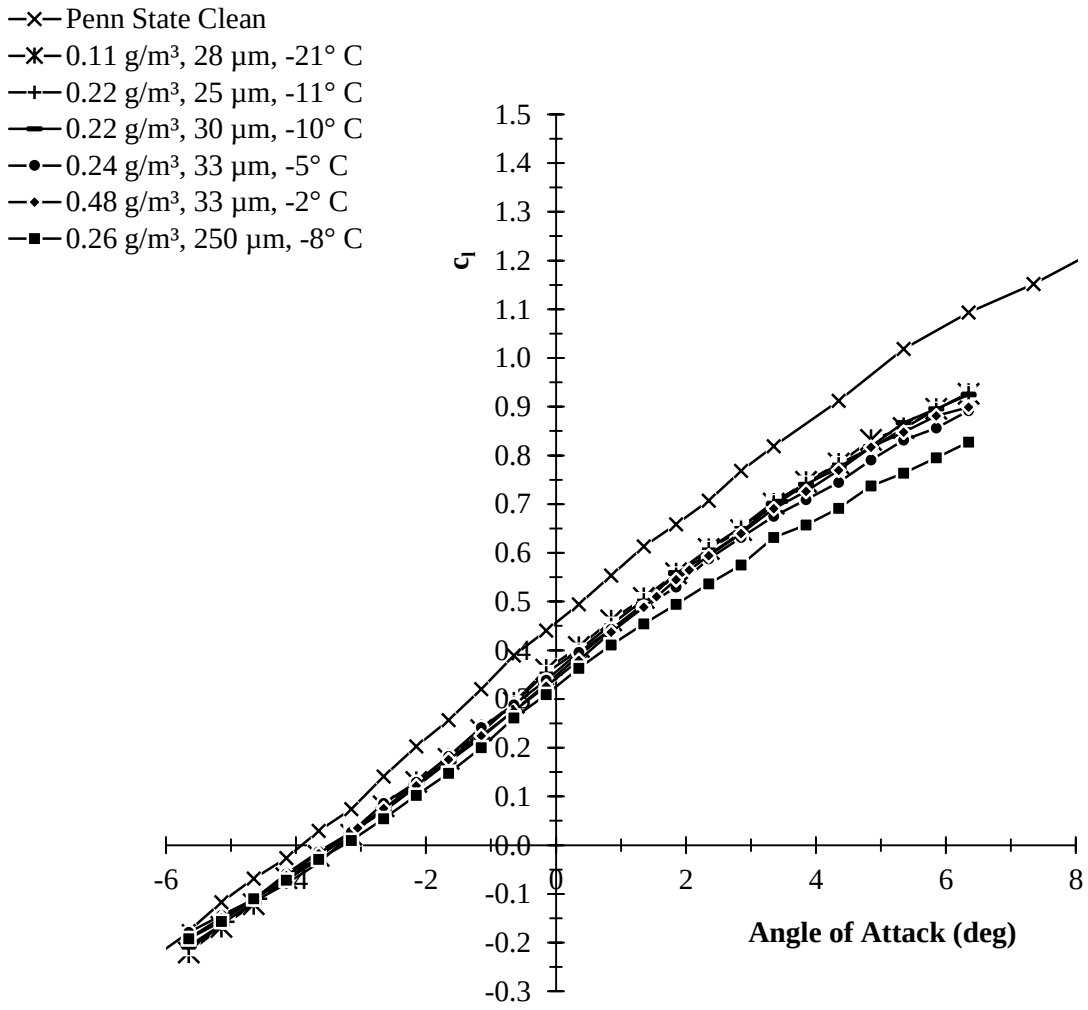

Figure 4-3. DU 93-W-210 airfoil: lift vs. angle of attack.

Variations in lift coefficient vs. drag coefficient for the six ice cases are displayed in Figures 4-4 and 4-5. The data displayed in Figure 4-4 are the actual load cell measurements after the wall interaction correction is made. The data in Figure 4-5 are an averaged fit of the data displayed in Figure 4-4. The standard deviation of the data set from the curves is 4% of the mean at lower lift coefficients and 6% of the mean at higher lift coefficients. Data from Figure 4-5 are used in the XTurb-PSU performance analysis. This is because the deviation between data points produces negligible changes when carried through calculations for wind turbine power output. The

data represented in Figure 4-5 are easier to use for performance analyses and do not affect the end results for power output.

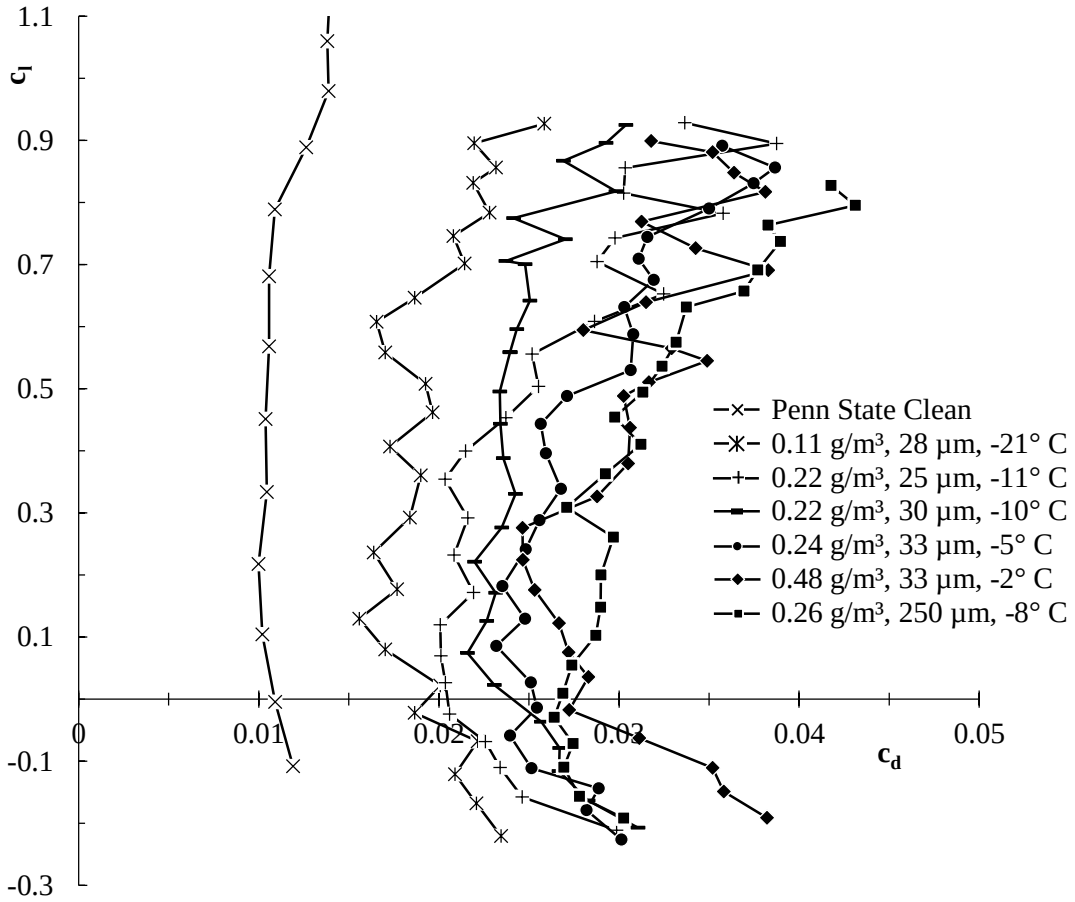

Figure 4-4. DU 93-W-210 airfoil: lift coefficient vs. drag coefficient.

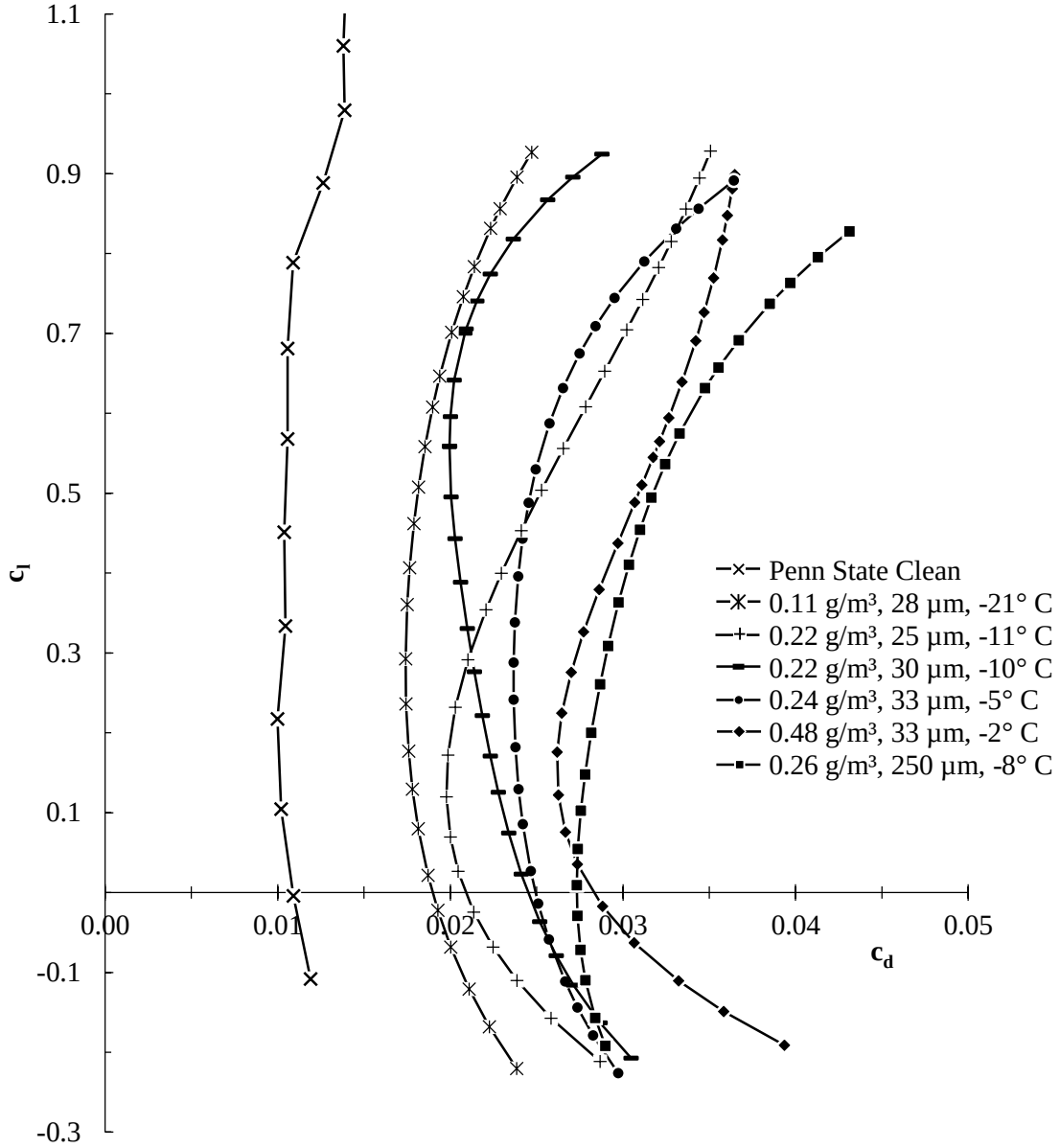

Figure 4-5. DU 93-W-210 airfoil: Curve fits of lift coefficient vs. drag coefficient.

The observed differences in drag between ice cases are a result of thickening of the boundary layer due to surface roughness elements [19]. The cases can be split into groupings of relatively low, medium, and high drag. The higher drag group contains cases that were warm temperature (close to 0° C) “glaze” ice in which ice is able to splash, run back, and generate

obtrusive ice feathers. The medium drag cases are a mix of rime and glaze ice with smaller roughness features than the warm temperature cases. These icing conditions are at a low enough temperature to not have runback ice, but do have ice feathers along the chord. The lowest drag ice case is pure rime ice at -21° C and is characterized by a thin coating of grit like roughness. The SLD case, in particular, has the highest drag at high lift due to the fact that it has the furthest ice impingement along the chord.

It is clear that temperature is a distinguishing factor between icing cases. For all cases except for the SLD case, drag increases with temperature. However, the shape of the drag curves is not easily correlated with temperature. In fact, the two cases at the nearly the same temperature (Cases 2 and 3 in Figure 4-5) are characterized by very different drag curves. The lift coefficient corresponding to minimum drag cases 2 and 3 are 0.12 and 0.55, respectively. Therefore, the correlation between drag increase and icing temperature is too complex to model with a simple approximation.

Drag increases by roughly 80% to 200% at low angles of attack and by up to 300% at higher angles of attack. Both the observed decrease in lift and increase in drag are on the same order as results of experiments on glaze ice and rime ice profiles by Hochart et al [10]. Tabulated polar data for all cases are available in Appendix B.

Power Prediction with XTurb-PSU

The DU 93-W-210 drag increases and lift losses described in the previous section yield a large reduction in local c_l/c_d in the operational angle of attack range of the PSU-Ice 1.5MW wind turbine. The reduction in performance significantly impacts wind turbine torque production. Power vs. wind speed for the PSU-Ice 1.5MW wind turbine operating at the same pitch settings in both

iced and baseline scenarios is displayed in Figure 4-6. Keeping the same pitch settings between cases gives a good visual representation of performance differences in Region III.

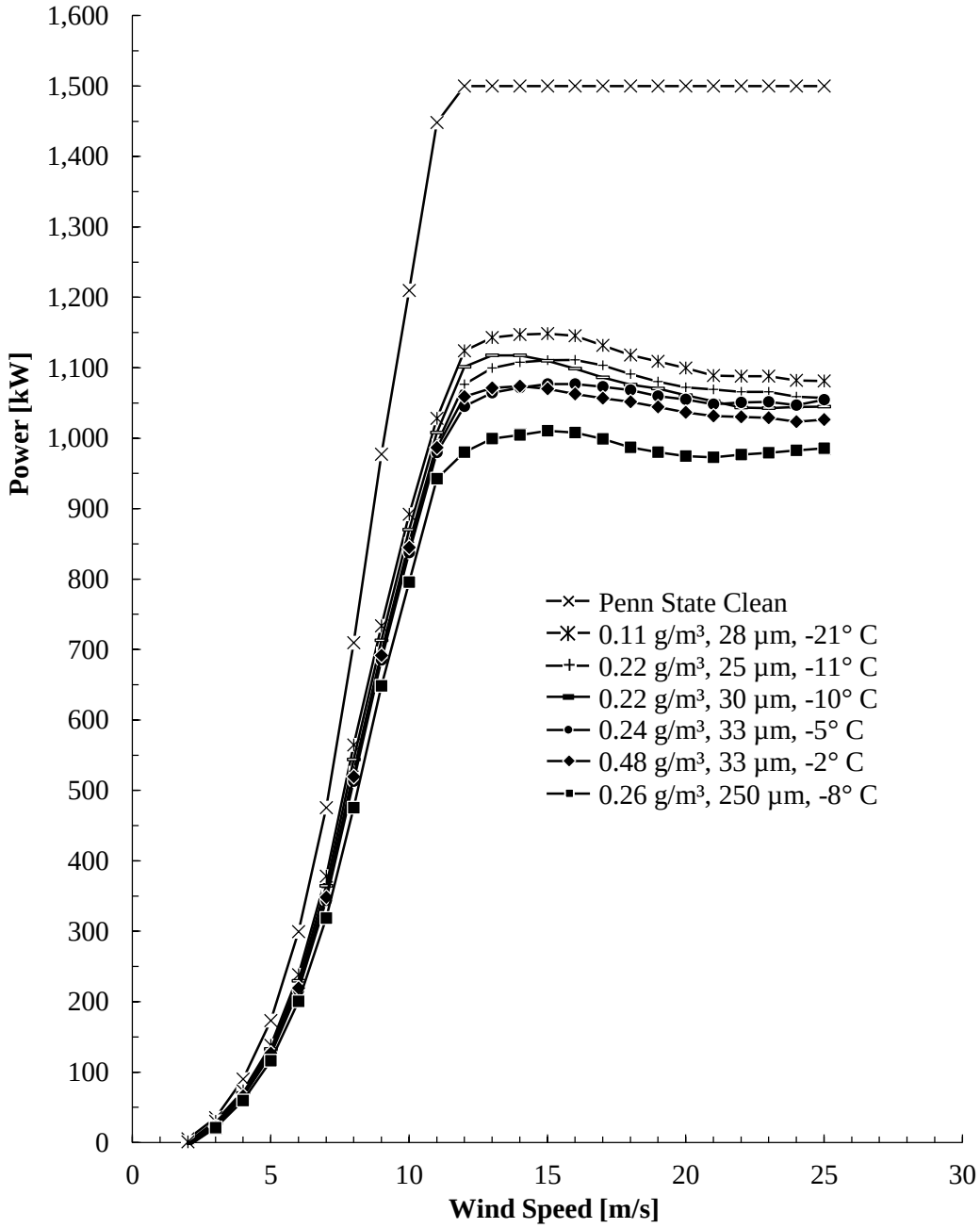

Figure 4-6. Power loss results from XTurb-PSU

A clear trend appears when observing temperature of ice cases versus power loss. Cold temperature rime ice yields the least amount of power loss whereas warm temperature glaze ice yields the largest power loss. This result is consistent with a study by Homola et al. in which "warmer" types of ice caused the largest losses in power [12]. It is difficult to see distinguishing features between icing cases when the power curve is displayed over such a wide range of wind speed. However, the difference in angle of attack distribution for different wind speeds changes the impact of the icing conditions within separate power regions. Region II wind speeds typically put the blade at high angles of attack as displayed in Figure 4-7, whereas Region III are characterized by low angles of attack.

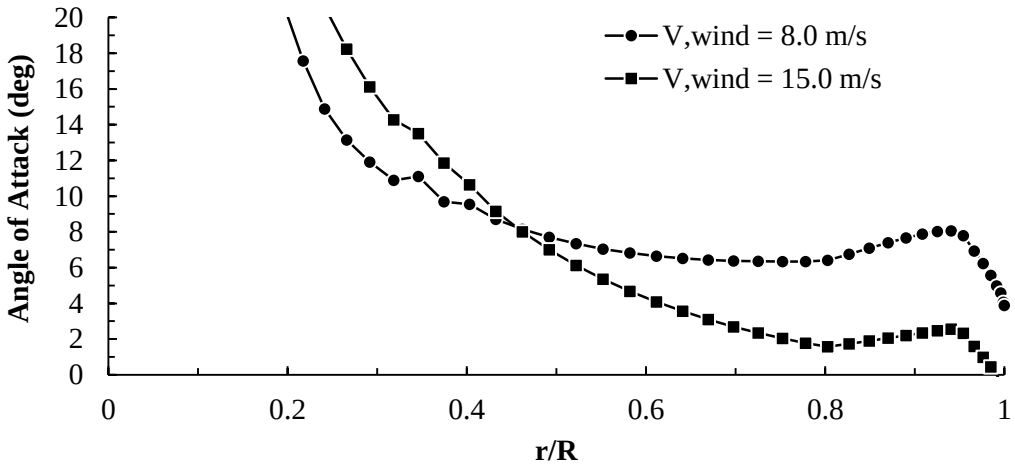

Figure 4-7. Angle of attack distributions for Region II and Region III wind speeds.

The power loss specific to Region II is illustrated in Figure 4-8. In Region II, the mean angle of attack is high. In this case, drag between icing cases is less distinguished and cases with different properties are closely grouped together. The only large deviations are from the low temperature rime icing case and SLD icing case, which have significantly altered ice shapes

compared to the other ice cases. However, this is not the case when power losses are observed at a lower mean angle of attack in Region III.

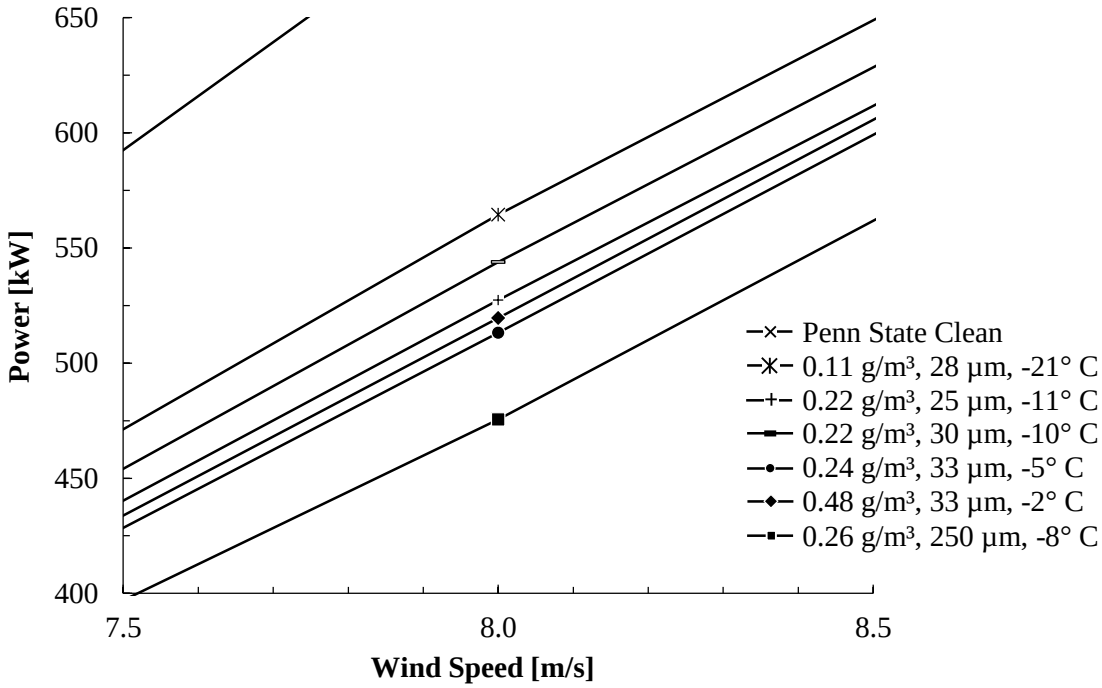

Figure 4-8. Power loss within Region II for the PSU-Ice 1.5MW wind turbine.

In Region III, power loss between the icing cases is more distinguished and cases are grouped by temperature. This is because the mean angle of attack is much lower in Region III. The airfoil is operating closer to its minimum drag, which is where the differences between airfoil drag are most pronounced. The two cases with similar conditions other than MVD (cases 3 and 4 in Table 2-3) do not show significant difference in power output. This is a useful observation because it indicates that MVD is not as important of a variable to consider in developing predictions for icing losses. An exceptional loss in power occurs for the SLD icing condition. These observations support the theory that surface roughness (and associated drag increase) results in the most dramatic differences in power output.

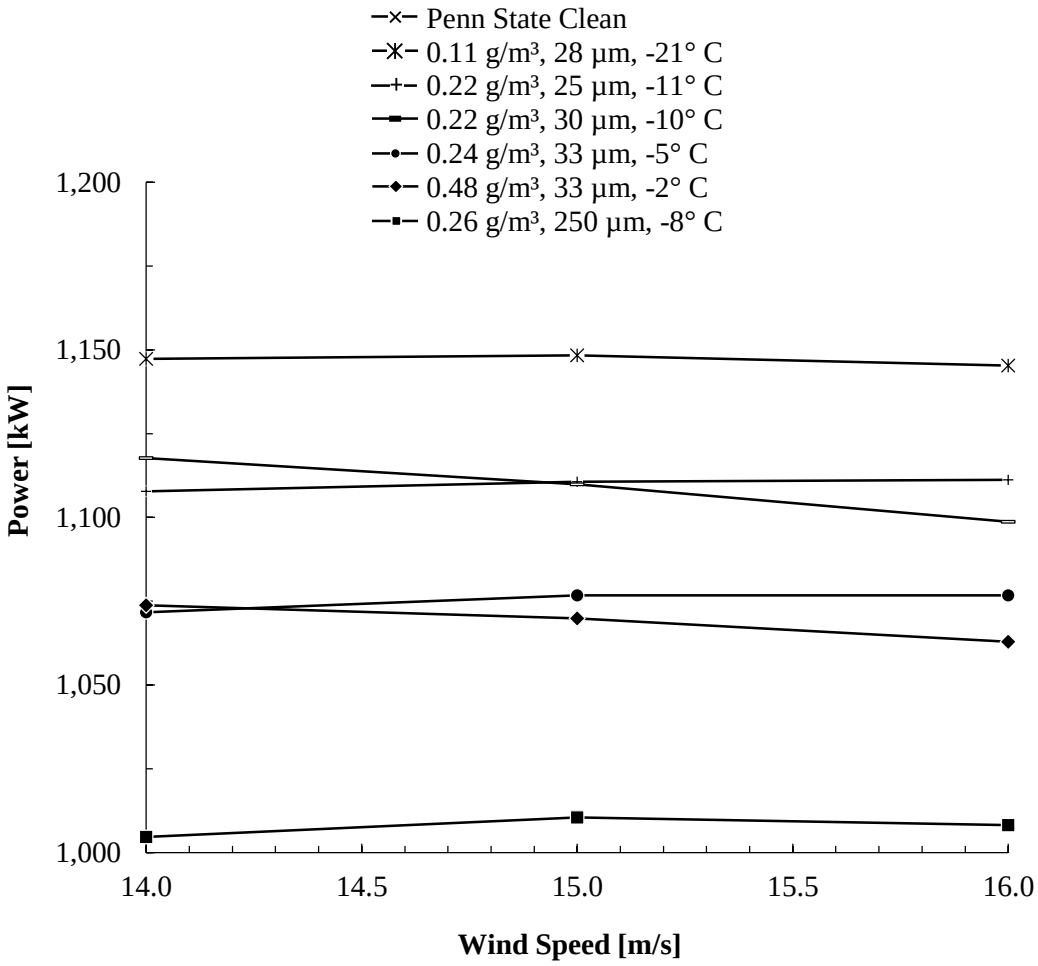

Figure 4-9. Power loss within Region III for the PSU-Ice 1.5MW wind turbine.

Power losses in Region II are substantial at roughly 20% for most icing conditions. Without any changes in pitch settings, the averaged losses increase to 25-30% throughout Region III. This agrees well with observations of Canadian wind energy sites in which "average power losses of 26% to 27% were observed" for similar meteorological conditions [8]. Similar losses are also reported by other experimental and computational studies [3, 11, and 15]. Detailed mean power loss percentages for regions II and III are displayed for each ice case in Table 4-3.

Table 4-3. Quantified Performance Penalties for each icing case.

Case	LWC (g/m^3)	MVD (μm)	T (°C)	Lift Loss (5° AoA)	Drag Increase (c_l = 0.5)	Mean Power Loss (Region II)	Mean Power Loss (Region III)
1	0.48	33	-2.3	14%	208%	21.8%	29.9%
2	0.24	33	-4.5	15%	181%	22.2%	28.6%
3	0.22	30	-9.7	15%	138%	17.8%	27.5%
4	0.22	25	-10.8	18%	152%	20.9%	27.5%
5	0.1	28	-21.3	15%	81%	15.9%	25.5%
6	0.26	250	-8.1	25%	219%	26.2%	33.8%

Discussion of Results

A multi-disciplinary experimental effort has yielded detailed aerodynamic performance data for an iced wind turbine airfoil (DU 93-W-210). The results have been used in wind turbine performance prediction and yielded a full set of power loss data for varying icing conditions (described in Table 2-3). The results encourage the opportunity for analysis and questioning of how these data can be used to improve current wind turbine operations and change future operations and/or wind turbine design.

Potential Correlations

Detailed iced airfoil results provide an opportunity to analyze potential correlations between icing parameters, flowfield parameters, performance changes, and iced airfoil geometry parameters. Airfoil lift degradation follows a similar trend for all freezing fog icing cases, so the iced airfoil lift loss is not dependent on any specific parameter for freezing fog icing cases. However, the SLD icing exhibits a higher lift loss than the freezing fog cases. The only significant change I parameters between the SLD and freezing fog icing cases is the extent of the ice impingement along the chord. Therefore, the loss of lift is directly correlated to ice impingement

limit. This supports the theory that the lift loss is due to a separation bubble whose size depends on the ice impingement limit [19].

Airfoil drag increase, on the other hand, does not behave similarly for similar icing conditions. The drag profiles are very diverse in shape and location of minimum drag coefficient for all icing conditions. A correlation exists between airfoil drag and temperature, but the magnitude of the drag increase is different for different lift coefficients and ice cases. No significant correlation exists between drag curves for varying ice impingement zone lengths (see Figure 4-1). The ice impingement zones are important to note, but the shape and size distribution of roughness elements within the zones are what truly create distinguishing features in the drag data. Although a correlation involving multiple icing parameters and drag rise may exist, it would require more data for validation.

Once airfoil data is integrated into power calculations, clear correlations between temperature and power loss exist. This is due to the general increase in drag coefficient for different icing conditions, which is more pronounced when integrated over an angle of attack range. However, even the power loss correlation changes with wind speed because the angle of attack range of the blade is changing. The relationship between power loss and temperature is still important because it provides a simple method to model first-order power loss for utility-scale wind turbines.

Operational Strategies for Optimal Performance

When an icing event occurs, the change in airfoil aerodynamics alters the optimal operation of the turbine. Optimizing wind turbine operations is a multi-disciplinary process that depends on icing conditions, icing event time, wind turbine performance, weather conditions before, during, and after the event, and the financial power market [2]. This research endeavors to find possible

strategies for improving performance that would change the outcome of the multi-disciplinary optimization process.

The first opportunity to gain more performance from an iced wind turbine is to optimize the pitch controller. This opportunity exists because the aerodynamic penalties yield a new aerodynamic model that has different optimal control settings than the original. Power output for a medium temperature (-10° C) rime/glaze icing condition (Case 3 in Table 2-3) with a comparison between original and optimized pitch settings is displayed in Figure 5-1. The optimal pitch settings yield small increases in Region II and recover power back to rated power in Region III. The new rated wind speed is about 4 m/s higher than the clean rated wind speed proving that iced wind turbines can still operate at a rated power range at high wind speeds.

Some wind turbines are already actively controlled for maximum power, but these controllers are tuned to the dynamics of a clean system. The performance of the controller in icing conditions could be improved by changing the dynamic model to include iced airfoil aerodynamics when icing is detected.

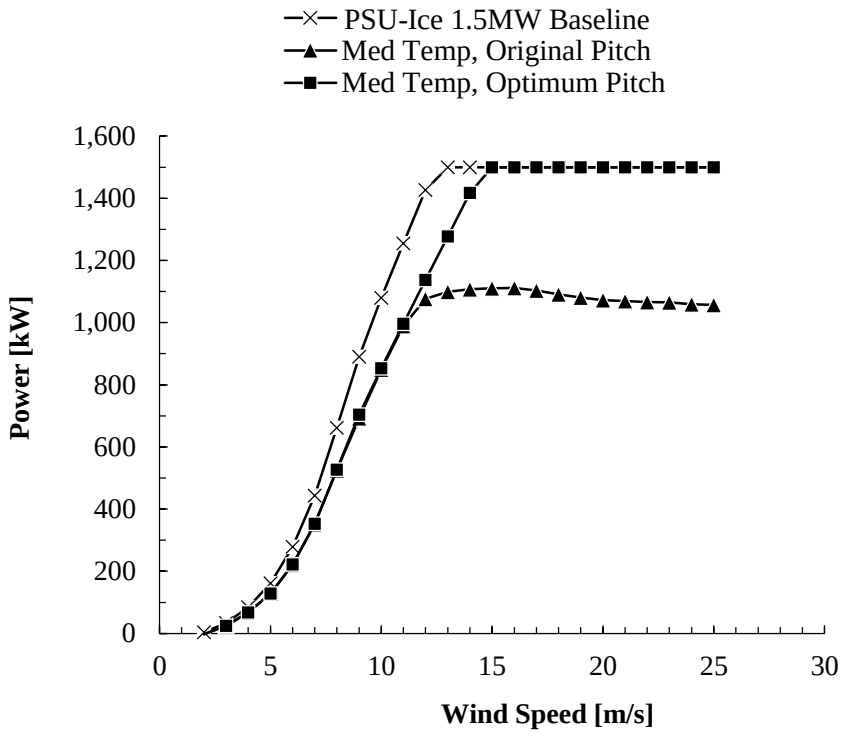

Figure 5-1. Power curve for optimally controlled pitch for icing Case 3 (Table 2-3)

Controlling power under iced conditions requires pitching the wind turbine blade less into the wind than normal. This change increases the loading on the wind turbine blade for a given wind speed, but the increased loads are still lower than "clean loads" due to the overall decrease in aerodynamic performance. The root-flap bending moment for optimal iced pitch settings displayed in Figure 5-2 is significantly lower than the maximum root-flap bending moment encountered at rated wind speed during baseline operation. It is therefore important to note that (disregarding ice shedding and loads due to ice weight) operating a wind turbine and pitching for optimal power in iced conditions does not exceed maximum baseline aerodynamic loads.

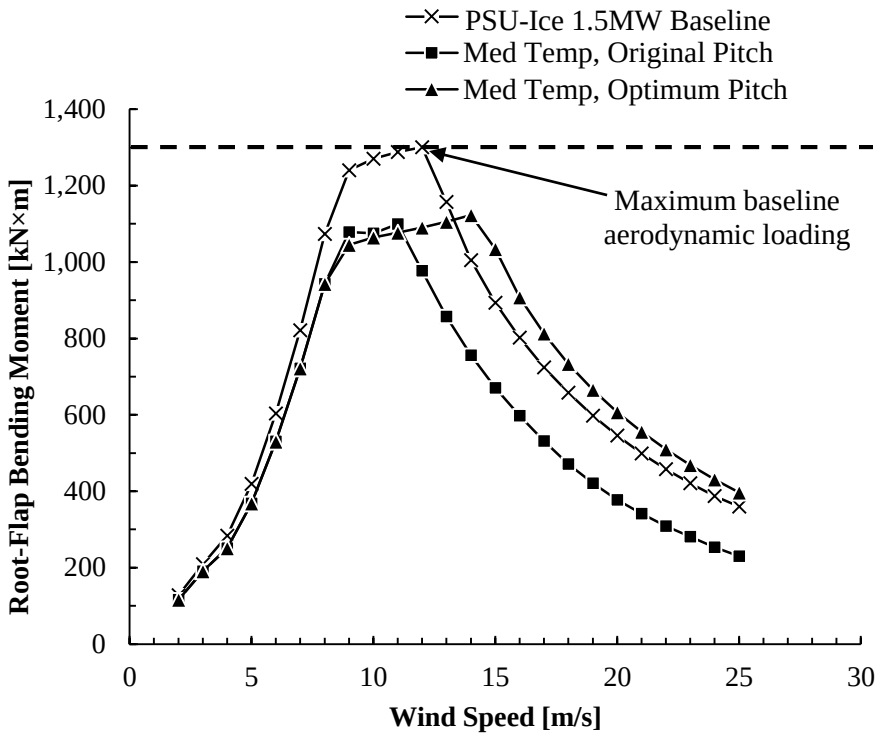

Figure 5-2. Root-flap bending moment for icing Case 3 (Table 2-3) at different pitch settings.

Other than changing the pitch-control settings of the wind turbine, there are not many options to optimize the aerodynamic operation of the wind turbine in the icing environment. However, there is still an opportunity to change operation of the wind turbine so that there is less of an aerodynamic penalty due to icing. Reducing local blade velocities by slowing the rotational rate of the rotor during an icing event could appreciably lower ice accretion and result in less performance loss after the icing event. However, there would be less power generation during the ice event when the rotor speed is slowed. There is a trade-off between power generated during and after the icing event, which depends on the duration of the icing event and expected wind resource post icing. This is a difficult trade-off to analyze since icing events are difficult to forecast, and the effectiveness of slowing the rotor to improve aerodynamic performance is not well understood.

More research is needed in this area to study how operational strategies could increase AEP for iced wind turbines.

Potential Applications of Data

A significant finding of this thesis is that surface roughness characteristics of iced airfoils has a leading order impact on airfoil drag. The impact of the roughness of the ice is much greater than that of the ice shape. It was mentioned in the introduction that many iced wind turbine performance prediction codes use simulated ice shapes with guesses at surface roughness parameters. This research offers detailed aerodynamic data for varying icing conditions as well as detailed geometric data for iced wind turbine airfoils. Other researchers can use this information to validate simulation results and obtain better predictions using complex solvers. This is important to do because wind site planners rely on accurate estimates of expected AEP loss due to icing when planning a wind energy site.

Chapter 5

Conclusion

A unique combination of ice accretion and wind-tunnel experiments yielded airfoil performance data for use in power prediction for a generic 1.5 MW wind turbine. Ice accretion experiments for six icing conditions were performed, and the ice shapes were molded and casted. These castings were mounted to a wind-tunnel model so that lift and drag could be measured for each icing condition. Finally, the lift and drag measurements were used as inputs to XTurb-PSU to calculate the power output of the iced PSU-Ice 1.5MW wind turbine.

Wind-tunnel experiments yielded a 16% decrease in lift common to all icing conditions. Large increases in drag are also observed, but varied across icing conditions from 80% to 220%. The variance in drag is due to differences in surface roughness between temperatures, resulting in higher drag for warm temperatures and lower drag for cold temperatures. The airfoil under SLD icing conditions exhibited particularly poor performance compared to freezing fog icing conditions. The observations of variation in drag due to roughness elements and measurements of roughness geometry are critical to developing better models for power-loss prediction in future work and could significantly contribute to future computational studies in the wind turbine icing community.

For a 45 minute freezing fog icing event, mean power loss on the PSU-Ice 1.5MW wind turbine ranged from 16% to 22% in Region II. Power loss increased for increasing temperatures and LWCs, but was relatively unchanged by changes in MVD. Power loss for an SLD icing event of the same duration is worse at 26% due to severely degraded airfoil performance. Further analysis of wind turbine aerodynamics showed that power output could be improved with changes in pitch settings. Pitch control can recover rated power in Region III at a rated wind speed 4 m/s higher than the original. This is accomplished without loading the wind turbine beyond maximum baseline aerodynamic loads, specifically the root-flap bending moment.

The data obtained in this thesis can provide other researchers with detailed aerodynamic information for wind turbine airfoils under varying icing conditions. The surface roughness geometry measurements provide a more accurate model for simulating icing roughness, while iced airfoil polars provide validation data for icing performance simulations. This research also has applications to the wind industry by providing wind turbine operators with basic power loss data that could be used to perform trade studies on optimizing wind farm operations in cold-climate conditions.

Future Work

This research effort was in no way a distinctly well-defined process from start to finish. Many questions developed throughout the research task that are worth pursuing. Opportunities for future work mostly involve additional testing using the same methods described in Chapter 3. However, there are also opportunities for research based on findings from this study.

There can never be enough experimental data points. This study focuses on a single blade span location and integrates measurements from this location across the entire blade span. A study by Hochart et al. found that icing penalties change significantly from root to tip of a wind turbine blade [10]. Experimentation on other blade sections with different airfoils, chord sizes, and local flow conditions could build a complete dataset, which would allow a more accurate prediction of power when integrating along the blade span.

This study proved decisively that significant drag differences can be seen between airfoils with the same shape but different surface roughness. Since surface roughness is the most important parameter for predicting airfoil drag, there could be significant work to study how to best replicate icing roughness on wind turbine blades numerically or even empirically. The physics are very complex and the geometries are difficult to model. Research that provides shortcuts in dealing with

the surface roughness problem would be very useful to the wind turbine aerodynamics and wind-energy community.

A major area of concern for optimizing wind turbine operations during an icing event is power loss as a function of time. There is hardly any research available on this subject for wind turbines, but an undeniable opportunity to improve operation schemes for iced wind turbines exists, if the time variance is tested and known. Measuring performance data for iced airfoils over a time interval could also be used to validate simulations of wind turbine icing.

This thesis set the focus on quantification of power losses, but did not attempt to search for wind turbine design changes to combat these power losses. There are many options for passive and active de-icing systems that have been thoroughly researched for aircraft and rotorcraft, but are less researched for application to wind turbines. For example, the data found in this study could be used to estimate how effective a heated blade might be in gaining back power losses during an icing event.

Wind turbine aerodynamics is a small field with even smaller resources available for research. However, the research performed in this thesis was fascinating, challenging, and yielded results that have direct applications to real-world problems. The author cannot think of a better outcome than this from a research project and hopes that work in this area will continue.

References

[1] Saidur, R., Islam, M. R., Rahim, N. A., and Solangi, K. H., "A Review on Global Wind Energy Policy." *Renewable and Sustainable Energy Reviews* (2010): 1744-1762.

[2] Laakso, Timo, Baring-Gould, I., Durstewitz, M., Horbaty, R., Lacroix, A., Peltola, E., Ronsten, G., Tallhaug, L., and Wallenius, T., "State-of-the-Art of Wind Energy in Cold Climates." *VTT Working Papers 152* (2010).

[3] Barber, S., Wang, Y., Jafari, S., Chokani, N., and Abhari, R. S., "The Impact of Ice Formation on Wind Turbine Performance and Aerodynamics". *Journal of Solar Energy Engineering* 133(1) 011007 (2011).

[4] Baring-Gould, Ian, Tallhaug, L., Ronsten, G., Horbaty, R., Cattin, R., Laasko, T., Durstewitz, M., Lacroix, A., Peltola, E., and Wallenius, T., "Recommendations for Wind Energy in Cold Climates." *VTT Working Papers 151* (2010).

[5] Byrkjedal, Øyvind, and Vindteknikk, K., "Estimating Wind Power Production Loss Due to Icing." *13th Int. Workshop on Atmospheric Icing*, Andermatt, Switzerland (2009).

[6] Fortin, Guy, and Perron, J., "Wind Turbine Icing and De-Icing." *47th AIAA Aerospace Sciences Meeting Including the New Horizons Forum and Aerospace Exposition*, Orlando, Florida (2009).

[7] Fu, Ping, and Farzaneh, M., "A CFD Approach for Modeling the Rime-Ice Accretion Process on a Horizontal-Axis Wind Turbine." *Journal of Wind Engineering and Industrial Aerodynamics* 98.4 (2010): 181-188.

[8] Gillenwater, Daniel, Masson, C., and Perron, J., "Wind Turbine Performance during Icing Events." *46th AIAA Aerospace Sciences Meeting and Exhibit*, Reno, Nevada (2008).

[9] Han, Yiqiang, Palacios, J., and Schmitz, S., “Scaled Ice Accretion Experiments on a Rotating Wind Turbine Blade,” *Journal of Wind Engineering and Industrial Aerodynamics* 109 (2012): 55-67.

[10] Hochart, Clement, Fortin, G., Perron, J., and Ilinca, A., "Wind Turbine Performance under Icing Conditions.” *Wind Energy* 11.4 (2008): 319-333.

[11] Homola, Matthew C., Virk, M. S., Nicklasson, P. J., and Sundsbø, P. A., “Performance Losses Due to Ice Accretion for a 5 MW Wind Turbine.” *Wind Energy* 15.3 (2012): 379-389.

[12] Homola, Matthew C., Virk, M. S., Wallenius, T., and Sundsbø, P. A., "Effect of Atmospheric Temperature and Droplet Size Variation on Ice Accretion of Wind Turbine Blades." *Journal of Wind Engineering and Industrial Aerodynamics* 98.12 (2010): 724-729.

[13] Jasinski, William J., Noe, S. C., Selig, M. S., and Bragg, M. B., "Wind Turbine Performance under Icing Conditions." *Journal of Solar Energy Engineering* 120.1 (1998): 60-65.

[14] Jha, Pankaj K., Brillembourg, D., and Schmitz, S., "Wind Turbines Under Atmospheric Icing Conditions—Ice Accretion Modeling, Aerodynamics, and Control Strategies for Mitigating Performance Degradation." *47th AIAA Aerospace Sciences Meeting Including the New Horizons Forum and Aerospace Exposition*, Nashville, Tennessee, (2012).

[15] Seifert, Henry, and Richert, F., "A Recipe to Estimate Aerodynamics and Loads on Iced Rotor Blades." *Proceedings of Boreas IV*, Enontekiö, Hetta, Finland (1998).

[16] Switchenko, David, Habashi, W. G., Baruzzi, G., and Ozcer, I., "FENSAP-ICE Simulation of Complex Wind Turbine Icing Events, and Comparison to Observed Performance Data." *32nd ASME Wind Energy Symposium*, National Harbor, Maryland (2014).

[17] Parsons, Brian, Milligan, M., Zavadil, B., Brooks, D., Kirby, B., Dragoon, K., and Caldwell, J., "Grid Impacts of Wind Power: A Summary of Recent Studies in the United States." *Wind Energy* 7 no. 2 (2004): 87-108.

[18] Han, Yiqiang, and Palacios, J., "Analytical and Experimental Determination of Airfoil Performance Degradation due to Ice Accretion," *4th AIAA Atmospheric and Space Environments Conference*, New Orleans, Louisiana (2012).

[19] Bragg, Michael B., Broeren, A. P., and Blumenthal, L. A., "Iced-Airfoil Aerodynamics." *Progress in Aerospace Sciences* 41.5 (2005): 323-362.

[20] Chi, X., Li, Y., Chen, H., Addy, H. E., Choo, Y. K., and Shih, T. I. P., "A Comparative Study using CFD to Predict Iced Airfoil Aerodynamics." *43rd Aerospace Sciences Meeting and Exhibit*, Reno, Nevada (2005).

[21] Timmer, W.A., and Van Rooij, R. P. J. O. M., "Summary of the Delft University Wind Turbine Dedicated Airfoils." *Journal of Solar Energy Engineering* 125.4 (2003): 488-496.

[22] URL: http://geosci.uchicago.edu/~moyer/GEOS24705/Readings/GEA14954C15-MW-Broch.pdf

[23] Palacios, Jose, Han, Y., Brouwers, E., and Smith, E., "Icing Environment Rotor Test Stand Liquid Water Content Measurement Procedures and Ice Shape Correlation." *Journal of American Helicopter Society* JAHS-1562 57 (2) 022006-1-12 (2012).

[24] Ruff, G.A., "Analysis and Verification of the Icing Scaling Equations." AEDC-TR—85-30, vol. 1. (Rev.) (1986).

[25] Wright, W. "User's Manual for LEWICE Version 3.2." NASA/CR-2008-214255 (2008).

[26] Reehorst, A. L.; Richter, G. P. "New Methods and Materials for Molding and Casting Ice Formations," NASA TM-100126, Lewis Research Center: Washington, D.C. (1987).

[27] Medina, R. "Validation of The Pennsylvania State University Low-Speed, Low-Turbulence Wind Tunnel Using Measurements of the S805 Airfoil." Diss. MS Thesis, Department of Aerospace Engineering, Penn State University, University Park, Pennsylvania (1994).

[28] Katz, J., and Walters, R., "Investigation of Wind-Tunnel Wall Effects in High Blockage Testing." *33rd Aerospace Sciences Meeting and Exhibit*, Reno, Nevada (1995).

[29] Pope, A., and Harper, J., *Low-Speed Wind Tunnel Testing*, John Wiley & Sons, Inc., New York (1966): Chap. 6.

[30] Schmitz, S., "XTurb-PSU – A Wind Turbine Design and Analysis Tool." The Pennsylvania State University (2011).

[31] Moriarty, P.J. and Hansen, A.C., "AeroDyn Theory Manual." NREL/TP-500-36881, URL: http://www.nrel.gov/docs/fy05osti/36881.pdf (2005)

[32] Du, Zhaohui, and Selig, M. S., "A 3-D Stall-Delay Model for Horizontal Axis Wind Turbine Performance Prediction." *Proceedings of the 1998 ASME Wind Energy Symposium*, Reno, Nevada (1998).

[33] URL: http://www.nrel.gov/designcodes/preprocessors/airfoilprep

[34] Shin, Jaiwon, and Berkowitz, B., "Prediction of Ice Shapes and their Effect on Airfoil Drag." *Journal of aircraft* 31.2 (1994): 263-270.

[35] URL: https://www.youtube.com/watch?v=BZ2k01BR_z8

Appendix A

LEWICE Ice Accretion Plots

The six plots below are LEWICE [25] accretion predictions for the full-scale and facility-scale icing conditions for each experimental case. These plots show the expected variance in ice accretions between full scale conditions and experimental replication of these conditions. Note that all full-scale cases are at 5° angle of attack whereas all facility-scale cases are at 0° angle of attack. Most of the cases match well, but there is always some variance due to the difference in angle of attack between the real wind turbine blade and the icing facility. The causes a shift of the ice shape, but relative thickness of the ice accretions remain on the same order. This is important to note because a majority of the lift and drag penalties that stem from these ice shapes are due to the surface roughness of the shapes rather than the shape itself [16]. The warmer temperature cases do not match as well, but LEWICE is also not validated to predict these shapes [25].

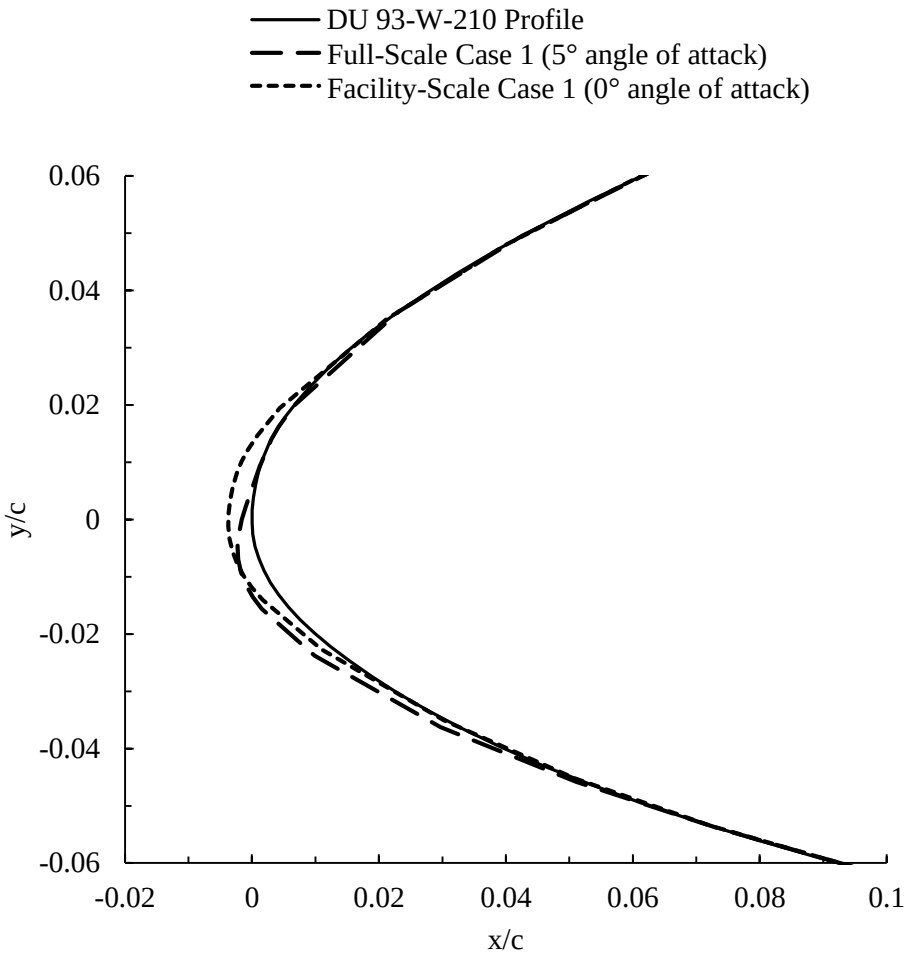

Figure A-1. Refer to Table 2-3: Case 1.

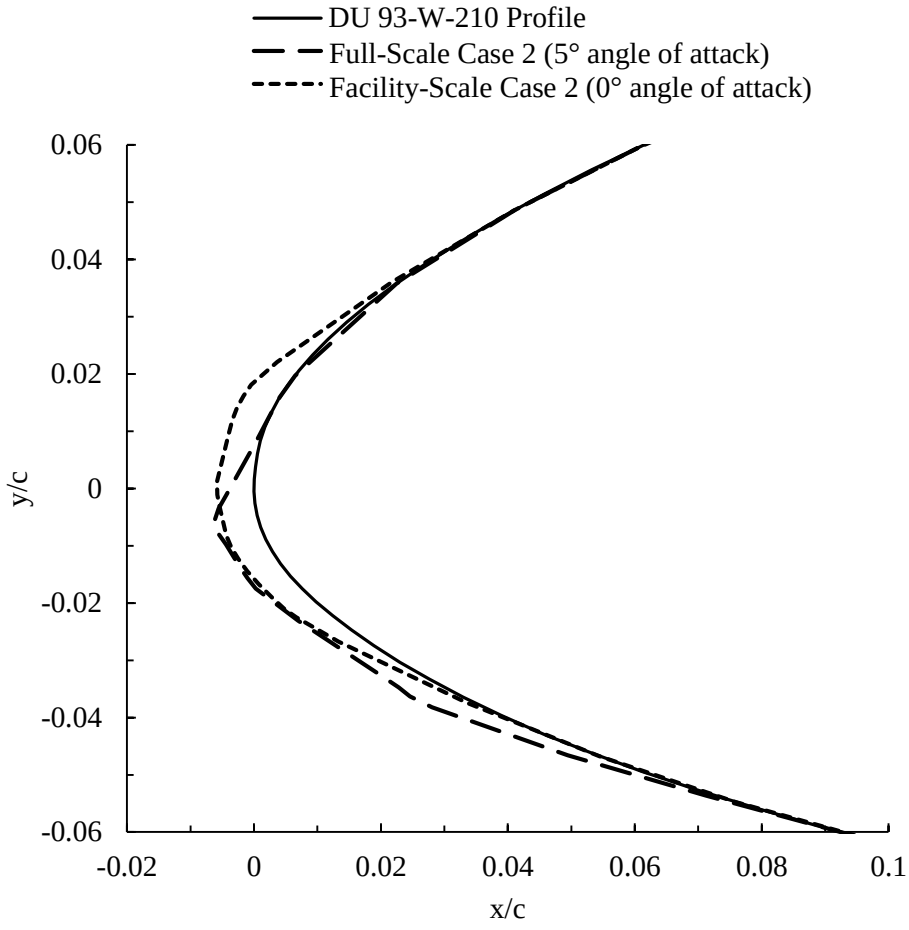

Figure A-2. Refer to Table 2-3: Case 2.

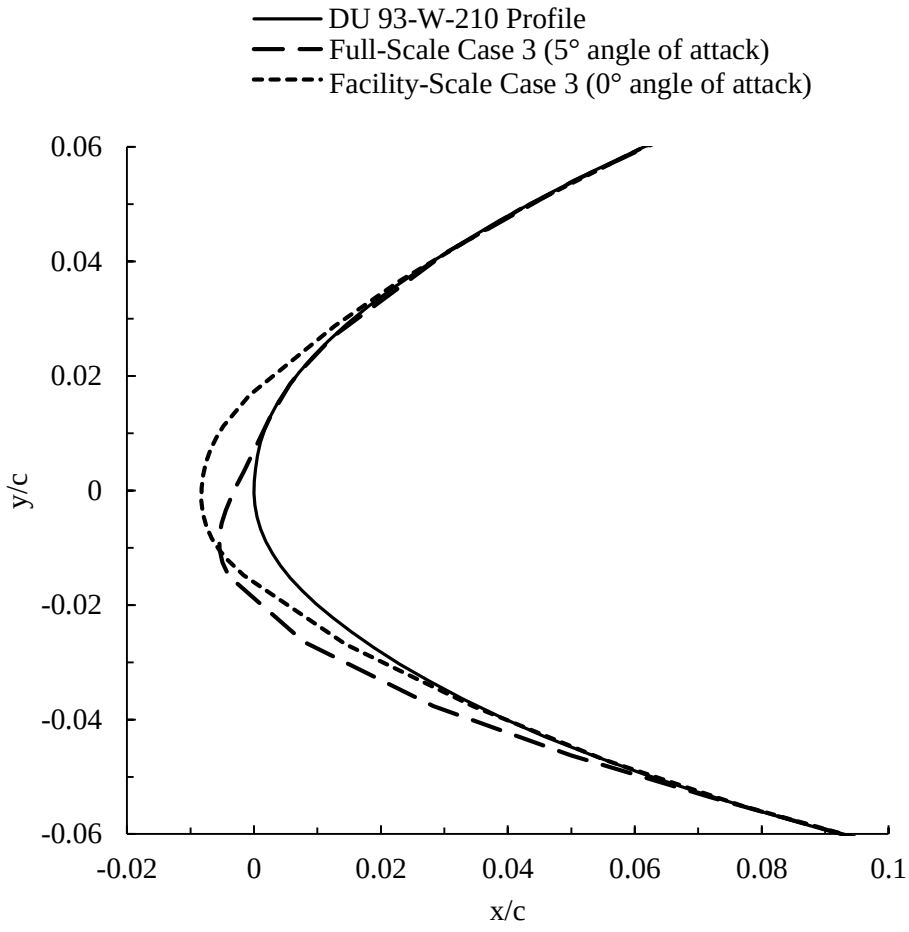

Figure A-3. Refer to Table 2-3: Case 3.

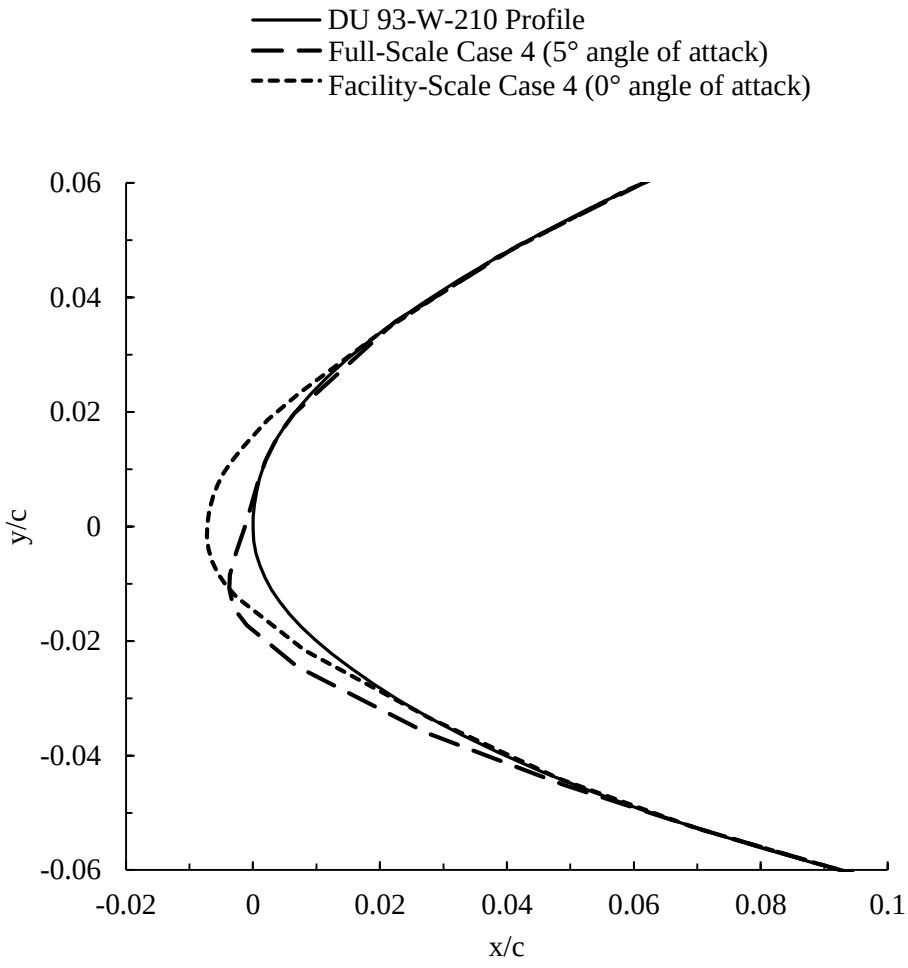

Figure A-4. Refer to Table 2-3: Case 4.

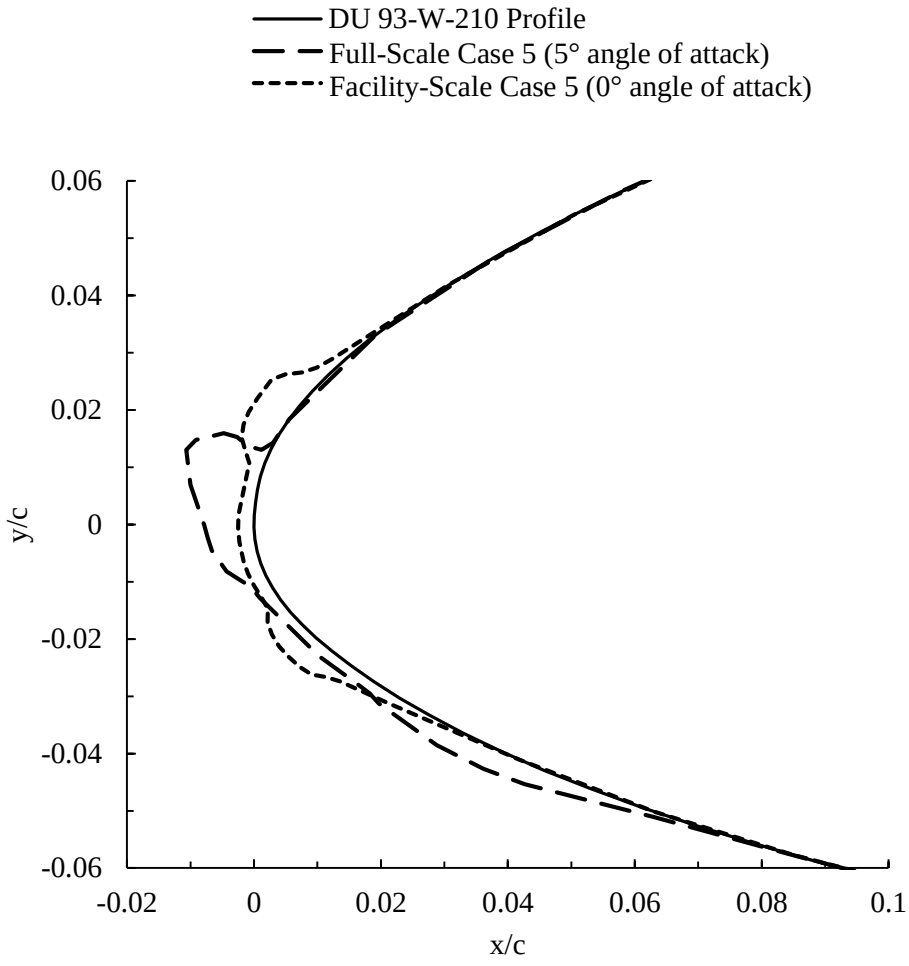

Figure A-5. Refer to Table 2-3: Case 5.

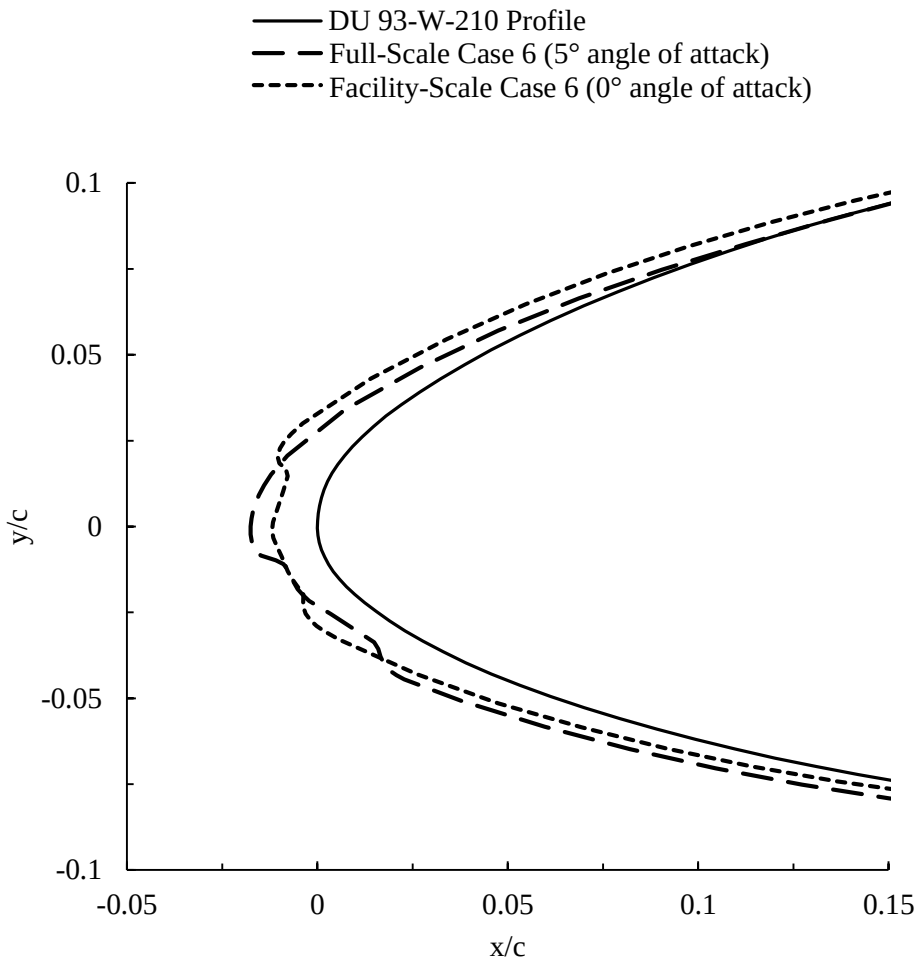

Figure A-6. Refer to Table 2-3: Case 6.

Appendix B

Iced Airfoil Tabulated Polar Data

Table B-1. Airfoil Polar Data for the clean DU 93-W-210 airfoil.

Alpha (deg)	c_l	c_d	c_m
-5	-0.1082	0.011905	N/A
-4	-0.0044	0.010905	N/A
-3	0.1043	0.010198	N/A
-2	0.2174	0.009990	N/A
-1	0.3337	0.010441	N/A
0	0.4513	0.010369	N/A
1	0.5679	0.010567	N/A
2	0.6811	0.010568	N/A
3	0.7886	0.010900	N/A
4	0.8885	0.012629	N/A
5	0.9793	0.013877	N/A
6	1.0599	0.013804	N/A
7	1.1302	0.013931	N/A
8	1.1905	0.013664	N/A
9	1.2420	0.016491	N/A
12	1.1600	0.060000	N/A
17	1.1800	0.140000	N/A

Table B-2. Airfoil Polar Data for case 1 (Table 2-3) for the DU 93-W-210 airfoil.

Alpha (deg)	c_l	c_d	c_m
-5.65	-0.2204	0.023843	N/A
-5.15	-0.1681	0.022264	N/A
-4.65	-0.1209	0.021088	N/A
-4.15	-0.0682	0.020024	N/A
-3.65	-0.0223	0.019281	N/A
-3.15	0.0215	0.018713	N/A
-2.65	0.0799	0.018142	N/A
-2.15	0.1295	0.017801	N/A
-1.65	0.1768	0.017582	N/A
-1.15	0.2360	0.017434	N/A
-0.65	0.2925	0.017408	N/A
-0.15	0.3606	0.017506	N/A
0.35	0.4066	0.017648	N/A
0.85	0.4617	0.017894	N/A
1.35	0.5076	0.018165	N/A
1.85	0.5581	0.018536	N/A
2.35	0.6076	0.018982	N/A
2.85	0.6464	0.019393	N/A
3.35	0.7014	0.020083	N/A
3.85	0.7458	0.020745	N/A
4.35	0.7835	0.021390	N/A
4.85	0.8317	0.022340	N/A
5.35	0.8561	0.022883	N/A
5.85	0.8956	0.023854	N/A
6.35	0.9267	0.024711	N/A
8	1.0000	0.026000	N/A
11	1.1000	0.070000	N/A

Table B-3. Airfoil Polar Data for case 2 (Table 2-3) for the DU 93-W-210 airfoil.

Alpha (deg)	c_l	c_d	c_m
-5.65	-0.2115	0.028675	N/A
-5.05	-0.1576	0.025835	N/A
-4.55	-0.1103	0.023858	N/A
-4.15	-0.0684	0.022470	N/A
-3.65	-0.0244	0.021355	N/A
-3.15	0.0265	0.020459	N/A
-2.65	0.0695	0.020001	N/A
-2.15	0.1198	0.019776	N/A
-1.65	0.1718	0.019857	N/A
-1.15	0.2317	0.020289	N/A
-0.65	0.2916	0.021025	N/A
-0.15	0.3540	0.022058	N/A
0.35	0.3996	0.022947	N/A
0.85	0.4532	0.024105	N/A
1.35	0.5037	0.025278	N/A
1.85	0.5558	0.026542	N/A
2.35	0.6083	0.027845	N/A
2.85	0.6525	0.028947	N/A
3.35	0.7045	0.030224	N/A
3.85	0.7426	0.031140	N/A
4.35	0.7826	0.032068	N/A
4.85	0.8152	0.032796	N/A
5.35	0.8556	0.033659	N/A
5.85	0.8946	0.034438	N/A
6.35	0.9283	0.035067	N/A
8	1.0000	0.037000	N/A
11	1.1000	0.070000	N/A

Table B-4. Airfoil Polar Data for case 3 (Table 2-3) for the DU 93-W-210 airfoil.

Alpha (deg)	c_l	c_d	c_m
-5	-0.1519	0.031787	N/A
-4	-0.0634	0.025479	N/A
-3	0.0336	0.020992	N/A
-2	0.1368	0.020453	N/A
0	0.3523	0.020298	N/A
1	0.4599	0.021571	N/A
2	0.5644	0.022616	N/A
3	0.6633	0.023788	N/A
4	0.7544	0.023811	N/A
5	0.8353	0.024423	N/A
6	0.9037	0.027622	N/A
7	0.9572	0.030460	N/A
8	1.0000	0.036000	N/A
11	1.1000	0.070000	N/A

Table B-5. Airfoil Polar Data for case 4 (Table 2-3) for the DU 93-W-210 airfoil.

Alpha (deg)	c_l	c_d	c_m
-6.15	-0.2261	0.029733	N/A
-5.65	-0.1790	0.028261	N/A
-5.15	-0.1440	0.027358	N/A
-4.65	-0.1114	0.026643	N/A
-4.15	-0.0588	0.025708	N/A
-3.65	-0.0137	0.025091	N/A
-3.15	0.0268	0.024657	N/A
-2.65	0.0857	0.024193	N/A
-2.15	0.1293	0.023955	N/A
-1.65	0.1820	0.023767	N/A
-1.15	0.2415	0.023668	N/A
-0.65	0.2881	0.023666	N/A
-0.15	0.3384	0.023742	N/A
0.35	0.3959	0.023933	N/A
0.85	0.4431	0.024190	N/A
1.35	0.4880	0.024531	N/A
1.85	0.5297	0.024952	N/A
2.35	0.5875	0.025736	N/A
2.85	0.6315	0.026521	N/A
3.35	0.6750	0.027490	N/A
3.85	0.7092	0.028405	N/A
4.35	0.7443	0.029508	N/A
4.85	0.7903	0.031238	N/A
5.35	0.8311	0.033084	N/A
5.85	0.8562	0.034376	N/A
6.35	0.8915	0.036423	N/A
8	1.0000	0.039000	N/A
11	1.1000	0.070000	N/A

Table B-6. Airfoil Polar Data for case 5 (Table 2-3) for the DU 93-W-210 airfoil.

Alpha (deg)	c_l	c_d	c_m
-5.65	-0.1911	0.039344	N/A
-5.15	-0.1489	0.035831	N/A
-4.65	-0.1107	0.033224	N/A
-4.15	-0.0630	0.030651	N/A
-3.65	-0.0174	0.028819	N/A
-3.05	0.0354	0.027365	N/A
-2.65	0.0755	0.026675	N/A
-2.15	0.1221	0.026253	N/A
-1.65	0.1758	0.026196	N/A
-1.15	0.2244	0.026463	N/A
-0.65	0.2757	0.027000	N/A
-0.15	0.3264	0.027724	N/A
0.35	0.3792	0.028619	N/A
0.85	0.4373	0.029699	N/A
1.35	0.4883	0.030681	N/A
1.55	0.5101	0.031100	N/A
1.85	0.5446	0.031752	N/A
2.05	0.5649	0.032126	N/A
2.35	0.5942	0.032650	N/A
2.85	0.6392	0.033415	N/A
3.35	0.6908	0.034211	N/A
3.85	0.7265	0.034707	N/A
4.35	0.7693	0.035241	N/A
4.85	0.8168	0.035756	N/A
5.35	0.8478	0.036051	N/A
5.85	0.8809	0.036333	N/A
6.35	0.8987	0.036472	N/A
8	1.0000	0.038000	N/A
11	1.1000	0.070000	N/A

Table B-7. Airfoil Polar Data for case 6 (Table 2-3) for the DU 93-W-210 airfoil.

Alpha (deg)	c_l	c_d	c_m
-5.65	-0.1919	0.028980	N/A
-5.15	-0.1569	0.028388	N/A
-4.65	-0.1097	0.027826	N/A
-4.15	-0.0717	0.027540	N/A
-3.65	-0.0293	0.027369	N/A
-3.15	0.0093	0.027325	N/A
-2.65	0.0545	0.027386	N/A
-2.15	0.1025	0.027558	N/A
-1.65	0.1478	0.027801	N/A
-1.15	0.2001	0.028162	N/A
-0.65	0.2609	0.028672	N/A
-0.15	0.3088	0.029139	N/A
0.35	0.3631	0.029743	N/A
0.85	0.4105	0.030347	N/A
1.35	0.4541	0.030979	N/A
1.85	0.4946	0.031649	N/A
2.35	0.5364	0.032441	N/A
2.85	0.5748	0.033280	N/A
3.35	0.6316	0.034758	N/A
3.85	0.6571	0.035532	N/A
4.35	0.6915	0.036697	N/A
4.85	0.7372	0.038502	N/A
5.35	0.7634	0.039688	N/A
5.85	0.7954	0.041298	N/A
6.35	0.8276	0.043123	N/A
8	1.0000	0.046000	N/A
11	1.1000	0.070000	N/A

Appendix C

XTurb-PSU Input Files

1. PSU 1.5MW Wind Turbine

```
&BLADE
   Name       = 'PSU 1.5MW',

   BN         = 3,

   ROOT       = 0.0444,


   NTAPER     = 10,

   RTAPER     = 0.0444,
            0.06,
            0.1,
            0.15,
            0.2,
            0.25,
            0.94,
            0.97,
            0.99,
            1.0,

   CTAPER     = 0.05333,
            0.05333,
            0.05889,
            0.06667,
            0.07111,
            0.07333,
            0.02889,
            0.02556,
            0.02000,
            0.01111,

   NTWIST     = 5,

   RTWIST     = 0.0444,
            0.15,
            0.8,
            0.95,
            1,

    DTWIST    = 10,
            10,
            2.75,
```

```
      -1.5,
      1.0,

NAIRF    = 10,

RAIRF    = 0.0444,
      0.09,
      0.11,
      0.13,
      0.15,
      0.18,
      0.4,
      0.5,
      0.6,
      0.825,

AIRFDATA =  './Cylinder.polar',
      './Cylinder1.polar',
      './Cylinder7.polar',
      './Cylinder9.polar',
      './00W240103.polar',
      './00W235003.polar',
      './97W30003.polar',
      './91W225003.polar',
      './93W21003.polar',
      './95W18003.polar',

BLENDAIRF  = 1,
 RMIN    = 0.15,
 RMAX    = 1.0,
STALLDELAY = 0,
VITERNA    = 1,

NSWEEP   = 2,

RSWEEP   = 0.25,
           1.00,

LSWEEP   = 0.00,
           0.00,


NDIHED   = 2,

RDIHED   = 0.25,
           1.00,

LDIHED   = 0.00,
           0.00,
```

```
&END
&OPERATION
  CHECK    = 0,

  DESIGN   = 0,

    NTSR     = 16,
    BTSR     = 5,
    ETSR     = 20,

    NPITCH   = 11,
    BPITCH   = -10,
    EPITCH   = 10,


  ANALYSIS = 0,

    NANA     = 10,

    TSRANA   = 2,
               4,
               6,
               8,
               10,
               12,
               14,
               16,
               18,
               20,

    PITCHANA = 3.0,
               3.0,
               3.0,
               3.0,
               3.0,
               3.0,
               3.0,
               3.0,
               3.0,
               3.0,


  PREDICTION = 1,

    BRADIUS  = 38.50,

    RHOAIR   = 1.225,

    MUAIR    = 1.8E-05,
```

```
NPRE     = 24,

VWIND    = 2,
       3,
       4,
       5,
       6,
       7,
       8,
       9,
       10,
       11,
       12,
       13,
       14,
       15,
       16,
       17,
       18,
       19,
       20,
       21,
       22,
       23,
       24,
       25,

RPMPRE   = 6.875,
       6.875,
       6.875,
       8.19,
       9.83,
       11.47,
       13.11,
       13.75,
       13.75,
       13.75,
       13.75,
       13.75,
       13.75,
       13.75,
       13.75,
       13.75,
       13.75,
       13.75,
       13.75,
       13.75,
       13.75,
       13.75,
       13.75,
       13.75,
```

```
          13.75,
          13.75,
          13.75,

    PITCHPRE = 0,
          0,
          0,
          0,
          0,
          0,
          0,
          0,
          0,
          0,
          2.79,
          6.78,
          9.55,
          11.88,
          13.95,
          15.84,
          17.60,
          19.26,
          20.84,
          22.34,
          23.79,
          25.18,
          26.51,
          27.8,

&END
&SOLVER
 METHOD    = 1,
   JX      = 41,
  COSDISTR = 1,
   GNUPLOT = 2,
&END
&HVM
  JJC = 1,
  AVISC = 0.5,
&END
&BEMT

&END
```

2. PSU-Ice 1.5MW Baseline Wind Turbine

The input files for the iced airfoil cases are the same as the input file listed below except that the airfoil polar file for the DU 93-W-210 airfoil is changed out for the iced airfoil polar file listing data that is displayed in the polar tables in Appendix C.

```
&BLADE
   Name        = 'PSU-Ice 1.5MW',

   BN          = 3,

   ROOT        = 0.0444,


   NTAPER      = 10,

   RTAPER      = 0.0444,
           0.06,
           0.1,
           0.15,
           0.2,
           0.25,
           0.94,
           0.97,
           0.99,
           1.0,

   CTAPER      = 0.05333,
           0.05333,
           0.05889,
           0.06667,
           0.07111,
           0.07333,
           0.02889,
           0.02556,
           0.02000,
           0.01111,

   NTWIST      = 5,

   RTWIST      = 0.0444,
           0.15,
           0.8,
           0.95,
           1,

    DTWIST     = 10,
           10,
```

```
      2.75,
      -1.5,
      1.0,

   NAIRF    = 7,

   RAIRF    = 0.0444,
      0.09,
      0.11,
      0.13,
      0.15,
           0.18,
           0.4,

   AIRFDATA =  './Cylinder.polar',
      './Cylinder1.polar',
      './Cylinder7.polar',
      './Cylinder9.polar',
           './00W240103.polar',
           './00W235003.polar',
      './93W21003.polar',

   BLENDAIRF  = 1,
    RMIN    = 0.15,
    RMAX    = 1.0,
   STALLDELAY = 0,
   VITERNA    = 1,

   NSWEEP   = 2,

   RSWEEP   = 0.25,
              1.00,

   LSWEEP   = 0.00,
              0.00,


   NDIHED   = 2,

   RDIHED   = 0.25,
              1.00,

   LDIHED   = 0.00,
              0.00,


&END
&OPERATION
  CHECK    = 0,
```

```
DESIGN   = 0,

  NTSR     = 29,
  BTSR     = 2,
  ETSR     = 16,

  NPITCH   = 21,
  BPITCH   = 0,
  EPITCH   = 10,


ANALYSIS = 0,

  NANA     = 10,

  TSRANA   = 2,
             4,
             6,
             8,
             10,
             12,
             14,
             16,
             18,
             20,

  PITCHANA = 3.0,
             3.0,
             3.0,
             3.0,
             3.0,
             3.0,
             3.0,
             3.0,
             3.0,
             3.0,


PREDICTION = 1,

  BRADIUS  = 38.50,

  RHOAIR   = 1.225,

  MUAIR    = 1.8E-05,


  NPRE     = 24,

  VWIND    = 2,
```

```
      3,
      4,
      5,
      6,
      7,
      8,
      9,
      10,
      11,
      12,
      13,
      14,
      15,
      16,
      17,
      18,
      19,
      20,
      21,
      22,
      23,
      24,
      25,

RPMPRE   = 6.875,
      6.875,
      6.875,
      8.19,
      9.83,
      11.47,
      13.11,
      13.75,
      13.75,
      13.75,
      13.75,
      13.75,
      13.75,
      13.75,
      13.75,
      13.75,
      13.75,
      13.75,
      13.75,
      13.75,
      13.75,
      13.75,
      13.75,
      13.75,
      13.75,

PITCHPRE = 0,
```

```
          0,
          0,
          0,
          0,
          0,
          0,
          0,
          0,
          0.2,
          7.465,
          10.83,
          13.56,
          15.945,
          18.11,
          20.112,
          21.975,
          23.74,
          25.425,
          27.02,
          28.54,
          30,
          31.415,
          32.765,

&END
&SOLVER
 METHOD    = 1,
   JX      = 51,
  COSDISTR = 1,
   GNUPLOT = 2,
&END
&HVM
  JJC = 1,
  AVISC = 0.5,
&END
&BEMT

&END
```

Appendix D

Ice Casting Photographs

This appendix contains photographs of the surface roughness for each case as well as a photo of all ice castings.

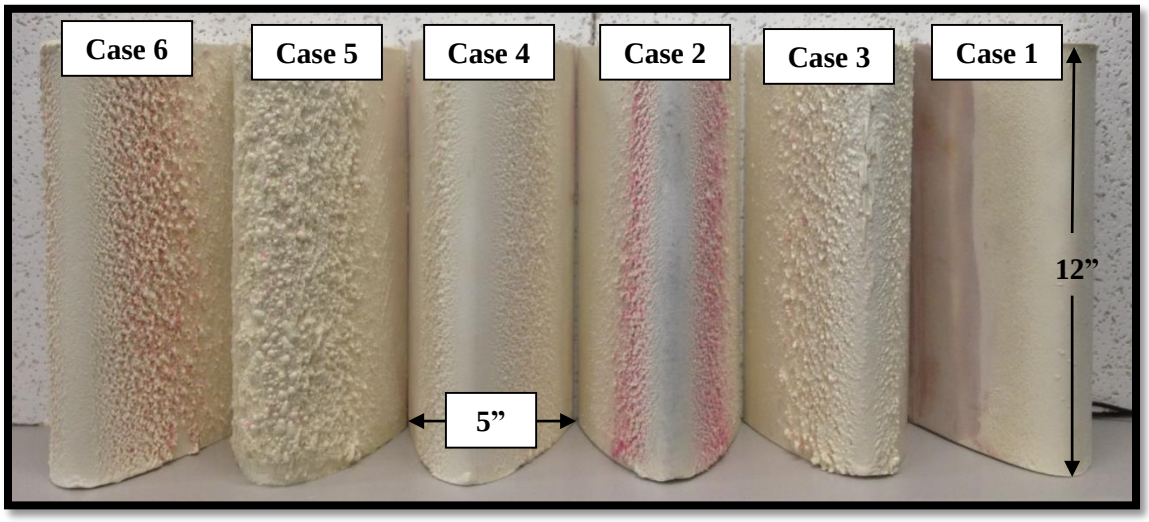

Figure D-1. Ice castings. From left to right: Cases (Table 2-3) 6, 5, 4, 2, 3, 1.

Figure D-2. Surface roughness detail. Refer to Table 2-3: Case 1.

Figure D-3. Surface roughness detail. Refer to Table 2-3: Case 2.

Figure D-4. Surface roughness detail. Refer to Table 2-3: Case 3.

Figure D-4. Surface roughness detail. Refer to Table 2-3: Case 4.

Figure D-5. Surface roughness detail. Refer to Table 2-3: Case 5.

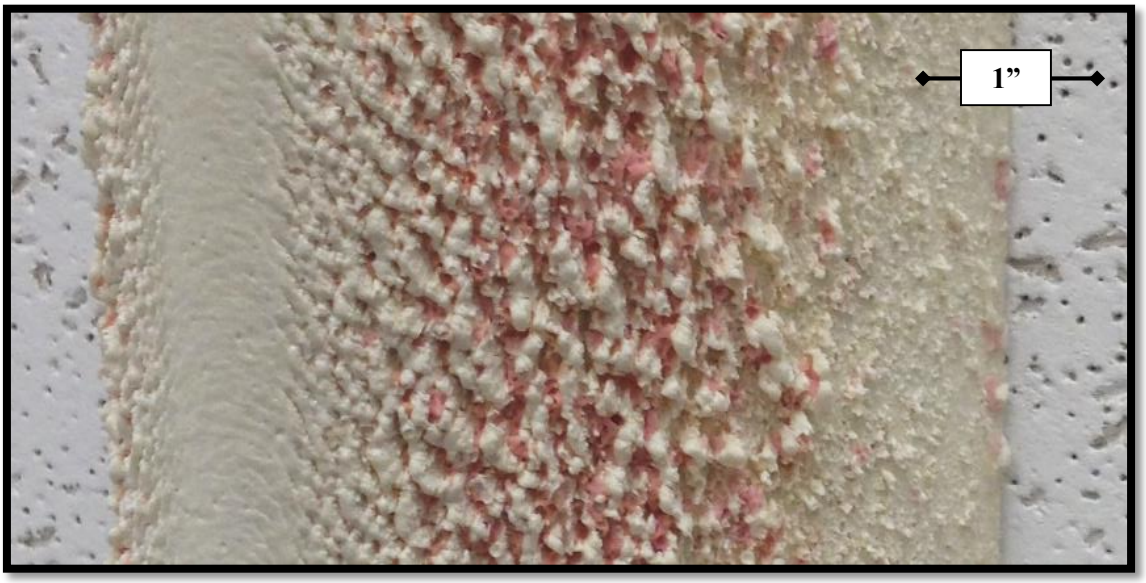

Figure D-6. Surface roughness detail. Refer to Table 2-3: Case 6.